ACS APPLIED MATERIALS & INTERFACES

Research Article

Cite This: ACS Appl. Mater. Interfaces 2020, 12, 1973−1987

www.acsami.org

Nanomagnet-Silica Nanoparticles Decorated with Au@Pd for Enhanced Peroxidase-Like Activity and Colorimetric Glucose Sensing

Omotayo Adeniyi,[†] Simbongile Sicwetsha,[†] and Philani Mashazi*[,†,‡]

[†]Department of Chemistry and [‡]Institute for Nanotechnology Innovation, Rhodes University, P.O. Box 94, Makhanda 6140, South Africa

Supporting Information

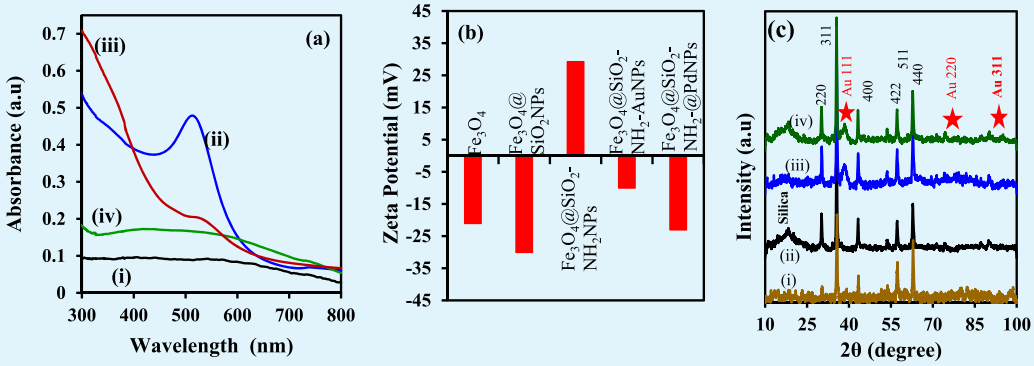

ABSTRACT: Nanomagnet-silica shell (Fe_3O_4@SiO_2) decorated with Au@Pd nanoparticles (NPs) were synthesized successfully. The characterization of Fe_3O_4@SiO_2-NH_2-Au@PdNPs was achieved using several spectroscopic and microscopic techniques. The quantitative surface analysis was confirmed using X-ray photoelectron spectroscopy. The Fe_3O_4@SiO_2-NH_2-Au@$Pd_{0.30}$NPs exhibited excellent peroxidase-like activity by effectively catalyzing the oxidation of 3,3′,5,5′-tetramethylbenzidine (TMB) in the presence of H_2O_2. The absorption peaks at 370 and 652 nm confirmed the peroxidase-like activity of the Fe_3O_4@SiO_2-NH_2-Au@$Pd_{0.30}$NPs. The Michaelis−Menten constant (K_m) of 0.350 and 0.090 mM showed strong affinity toward H_2O_2 and TMB at Fe_3O_4@SiO_2-NH_2-Au@$Pd_{0.30}$NPs. The mechanism of the peroxidase-like activity was found to proceed via an electron transfer process. A simple colorimetric sensor based on glucose oxidase and Fe_3O_4@SiO_2-NH_2-Au@$Pd_{0.30}$NPs showed excellent selectivity and sensitivity towards the detection of glucose. The fabricated glucose biosensor exhibited a wide linear response toward glucose from 0.010 to 60.0 μM with an limit of detection of 60.0 nM and limit of quantification of 200 nM. The colorimetric biosensor based on Fe_3O_4@SiO_2-NH_2-Au@$Pd_{0.30}$NPs as a peroxidase mimic was also successfully applied for the determination of glucose concentrations in serum samples. The synthesized Fe_3O_4@SiO_2-NH_2-Au@$Pd_{0.30}$NPs nanozymes exhibited excellent potential as an alternative to horseradish peroxidase for low-cost glucose monitoring.

KEYWORDS: *nanomagnets-silica, gold@palladium nanoparticles, peroxidase-like activity, nanozyme, glucose sensor*

INTRODUCTION

The recent advancement in nanozymology has offered enormous opportunity for developing nanostructured artificial enzymes. Nanozymes are nanomaterials that possess intrinsic enzyme-like activities.[1] In contrast to natural enzymes, nanozymes have tuneable and efficient enzyme-like activity, are produced at low cost, have high environmental stability, and are amenable to mass production.[2] These advantages have necessitated investigations of various nanomaterials with intrinsic peroxidase-like,[3−5] oxidase-like,[6,7] catalase-like,[8] and superoxide dismutase-like activities.[9] Nanozymes that mimic the enzyme-like activity of horseradish peroxidase (HRP) have been of great interest due to their application in bioanalytical and clinical chemistry. Nanozymes that posess peroxidase-like activity catalyze the oxidative reaction of various colorimetric substrates by transferring electron to H_2O_2.[10] Since the discovery of the peroxidase-like activity of Fe_3O_4 nanoparticles (NPs) in 2007 by Gao et al.,[11] different inorganic nanomaterials, including noble metals (e.g., Ag, Au, Pd, Pt),[5,12−15] transition-metal oxides and chalcogenides (e.g., FeS, CeO_2, V_2O_5, CuO, MoS_2),[16−19] metal−organic frameworks,[3,20−23] and carbon nanomaterials (carbon nanotubes, carbon dots, graphene quantum dots)[24−26] have been discovered to possess intrinsic similar properties. These nanomaterials oxidize substrates such as *o*-phenylenediamine, 2,2-azino-bis-(3-ethylbenzothiazoline-6-sulfonic acid), and 3,3′,5,5′-tetramethylben-

Received: August 28, 2019
Accepted: December 17, 2019
Published: December 17, 2019

DOI: 10.1021/acsami.9b15123
ACS Appl. Mater. Interfaces 2020, 12, 1973−1987

zidine (TMB) to the corresponding colored products in the presence of H_2O_2. Since the colorimetric response of peroxidase-like activity of nanozymes depends on the concentration of H_2O_2, this strategy has been used in the design of biosensors based on quantification of H_2O_2 generated or consumed in a biochemical reaction. This has provided a low-cost colorimetric assay for the detection of various disease biomarkers, including H_2O_2, glucose, dopamine, biothiols, and cancers. Nanozymes, which have peroxidase-like activity, are currently explored as alternatives to HRP in the design of versatile electrochemical and colorimetric biosensors.[27] However, known peroxidase-like nanozymes have much lower catalytic activity and poor selectivity in comparison with HRP.[4] Carbon nanomaterials, and metal oxide nanoparticles (NPs) are cheap but possess relatively lower peroxidase-like activity compared with HRP.[28] Interestingly, noble metal NPs have shown comparable to better peroxidase-like activity when compared with HRP.[6,9,10,12−15] However, they often express multiple enzyme-like activities and are expensive.[9,29] To exemplify this, it is worth mentioning that AuNPs,[9] Au@PtNPs,[6,30] and $NiCo_2O_4$[31] exhibit excellent oxidase-like and peroxidase-like activity. In the design of conventional glucose biosensor, a bienzyme cascade system consisting of glucose oxidase (GOx) and HRP is commonly used. GOx enzyme reaction produces H_2O_2 (as a by-product). HRP reduces the GOx produced H_2O_2 whilst itself being oxidased. The reduction of HRP occurs, and the oxidation of chromogen as a substrate then occurs. Nanozymes that possess peroxidase-like activity can replace HRP in this bienzyme cascade.

Methods that seek to control the size and shape, surface modification, crystal facet, and formation of nanohybrids and nanocomposite materials are investigated. Amongst the various methods, nanohybrids are particularly attractive due to the possible synergistic advantages of each component in achieving improved catalytic properties. Nanocomposites (GO-Fe_3O_4[17,25] and MoS_2/PtCu[32]) and nanohybrids (PB@FePt,[33] Cu@Pd/RGO,[34] CeO_2/NT-TiO_2[35]) have exhibited superior or new enzyme-like activity that cannot be achieved by either component alone. These results inspired the research into exploiting novel nanozymes with excellent peroxidase-like activity based on their magnetic properties and selectivity toward peroxidase substrates. In this study, we report novel Fe_3O_4@SiO_2-NH_2-Au@PdNPs as nanohybrids with enhanced peroxidase-like activity. The characterization, enzyme-like activity, and the mechanism for the improved peroxidase-like activity of Fe_3O_4@SiO_2-NH_2-Au@PdNPs were evaluated. Fe_3O_4@SiO_2-NH_2-Au@PdNPs were selective toward H_2O_2 and were evaluated toward colorimetric detection of glucose.

EXPERIMENTAL SECTION

Reagents, Instrumentation, and Procedure for Preparation of Solution. All reagents and solvents used in this study were of analytical grade and used as received from the suppliers. Ultrapure water with a resistivity of 18 MΩ cm obtained from a Milli-Q water system (Millipore Corp, Bedford, MA) was used for the preparation of all solutions. The details of the reagents and suppliers, instrumental analysis, and experimental procedures are presented in the Supporting Information (SI).

Synthesis of Fe_3O_4@SiO_2-NH_2-Au@PdNPs. Scheme 1 shows the schematic illustration for the preparation of Fe_3O_4@SiO_2-NH_2-Au@PdNPs. The detailed procedure and the amount of reagents used for the synthesis of Fe_3O_4@SiO_2-NH_2-Au@PdNPs are presented in SI. The preparation of Fe_3O_4@SiO_2-NH_2-Au@PdNPs involved three

Scheme 1. Schematic Illustration of the Synthesis of Fe_3O_4@SiO_2-NH_2-Au@PdNPs

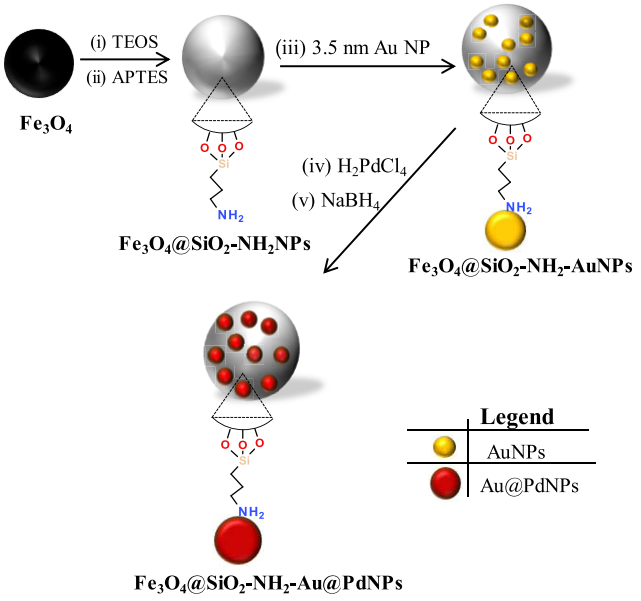

steps. First, highly monodispersed magnetic nanoparticles (Fe_3O_4) were synthesized by thermal decomposition of the iron−oleate complex in octadecene. The oleic acid-capped Fe_3O_4NPs were coated with silica shell using the water-in-oil microemulsion system to form silica-coated magnetite nanoparticles (Fe_3O_4@SiO_2NPs). The mechanism for the ligand exchange of the hydrophobic magnetic NPs by alkoxysilane within the water-in-oil microemulsion systems to obtain hydrophilic Fe_3O_4@SiO_2NPs has previously been reported.[36,37] The silica shell was covalently formed on the Fe_3O_4 core via the phase transfer of the oleic acid with hydrolyzed alkoxy groups of tetraethyl orthosilicate. The transfer of the hydrophilic silanol-capped magnetite into the water-in-oil-microemulsion nanoreactor occurs and the subsequent growth of the silica shell to form Fe_3O_4@SiO_2NPs. The Fe_3O_4@SiO_2NPs were isolated by breaking the microemulsion via pH adjustment to 2.0, periodic cooling in liquid nitrogen, and the addition of acetone.[36] The Fe_3O_4@SiO_2NPs were modified with (3-aminopropyl)triethoxysilane (APTES) to form amine-functionalized Fe_3O_4@SiO_2-NH_2NPs. The terminal $-NH_2$ functional groups for Fe_3O_4@SiO_2-NH_2 served as an anchor for the self-assembly of Au@PdNPs to form Fe_3O_4@SiO_2-NH_2-Au@PdNPs.

The second step involves the adsorption of 3.5 nm AuNPs on Fe_3O_4@SiO_2-NH_2NPs. The 3.5 nm AuNPs were dispersed onto the surface of the Fe_3O_4@SiO_2-NH_2NPs support via nitrogen−gold (Au−N) interactions. The color of the Fe_3O_4@SiO_2-NH_2NPs solution changed from dark gray to reddish-brown, confirming the adsorption of AuNPs onto Fe_3O_4@SiO_2-NH_2NPs to form Fe_3O_4@SiO_2-NH_2-AuNPs. The third step is the deposition of Pd onto the Fe_3O_4@SiO_2-NH_2-AuNPs to form Fe_3O_4@SiO_2-NH_2-Au@PdNPs. The formation of the Fe_3O_4@SiO_2-NH_2-Au@PdNPs was achieved via the seed-mediated method.[38−40] The Fe_3O_4@SiO_2-NH_2-AuNPs were dispersed in a solution of H_2PdCl_4, the sequential addition of low concentrations of $NaBH_4$ induces the homogenous reduction of Pd^{2+} onto the surface of the Fe_3O_4@SiO_2-NH_2-AuNPs. The homogenous reduction prevented the formation of new Pd nuclei in solution. The 3.5 nm AuNPs as gold seeds onto the Fe_3O_4@SiO_2-NH_2-AuNPs acted as the nucleation sites for the deposition of Pd^0, resulting in the formation of Fe_3O_4@SiO_2-NH_2-Au@PdNPs. The concentration of H_2PdCl_4 was varied to obtain Fe_3O_4@SiO_2-NH_2-Au@PdNPs with different contents of Pd. Each step of the synthesis was purified by washing with deionized water, sonication, and magnetic separation. The use of magnetic separation only afforded the adsorbed metal nanoparticles to be collected and analyzed further.

DOI: 10.1021/acsami.9b15123
ACS Appl. Mater. Interfaces 2020, 12, 1973−1987

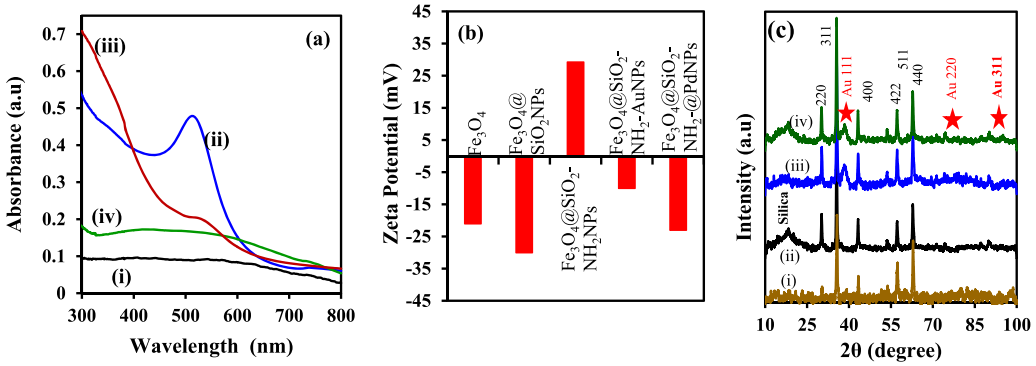

Figure 1. (a) UV−vis absorption spectra, (b) dynamic light scattering (DLS, ζ-potentials) and (c) X-ray diffractograms of the synthesized nanoparticles. For UV−vis (i) Fe_3O_4@SiO_2NPs, (ii) AuNPs, (iii) Fe_3O_4@SiO_2-NH_2-AuNPs, and (iv) Fe_3O_4@SiO_2-NH_2-Au@PdNPs; for (c) XRD pattern of (i) Fe_3O_4, (ii) Fe_3O_4@SiO_2-NH_2NPs (iii) Fe_3O_4@SiO_2-NH_2-AuNPs, and (iv) Fe_3O_4@SiO_2-NH_2-Au@PdNPs.

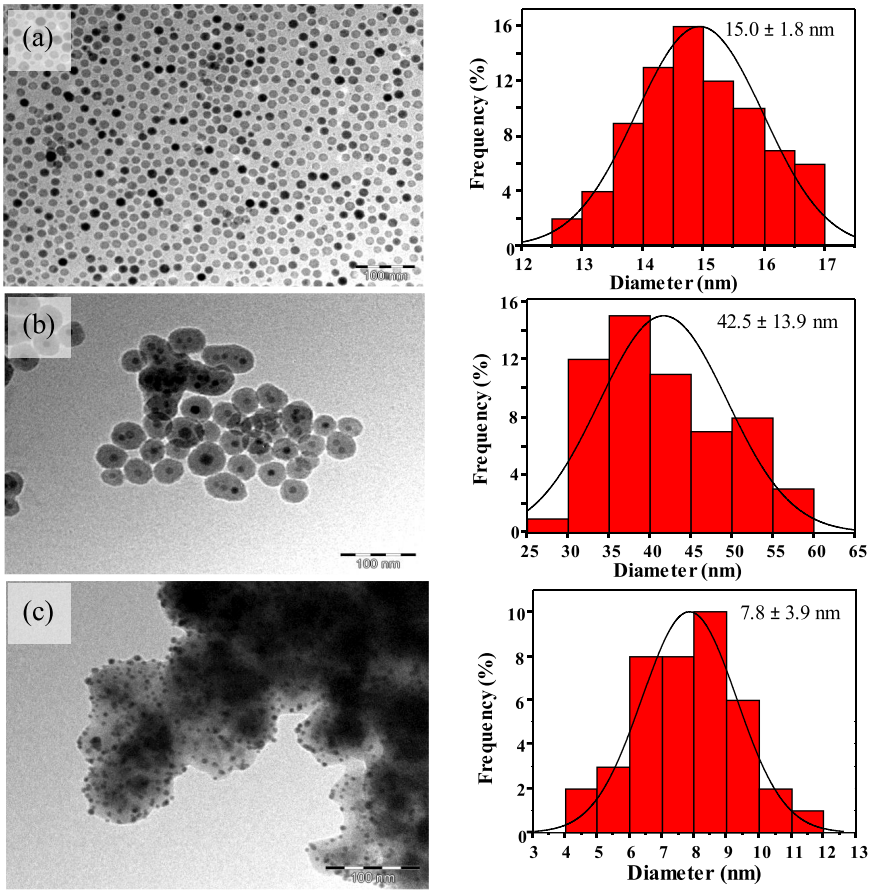

Figure 2. TEM micrographs with their corresponding size distribution histograms for (a) Fe_3O_4NPs, (b) Fe_3O_4@SiO_2-NH_2NPs, and (c) Fe_3O_4@SiO_2-NH_2-Au@PdNPs.

RESULTS AND DISCUSSION

Characterization of Fe_3O_4@SiO_2-NH_2-Au@PdNPs. The step-by-step synthesis of Fe_3O_4@SiO_2-NH_2-Au@PdNPs was followed using various techniques. Figure 1 shows (a) the UV−vis spectra, (b) dynamic light scattering (DLS, ζ-potential), and (c) X-ray diffractograms (XRD) for the synthesis of Fe_3O_4@SiO_2-NH_2-Au@PdNPs. The UV−vis spectra in Figure 1a shows spectra of (i) Fe_3O_4@SiO_2NPs, (ii) AuNPs, (iii) Fe_3O_4@SiO_2-NH_2-AuNPs, and (iv) Fe_3O_4@SiO_2-NH_2-Au@PdNPs. The UV−vis spectrum of Fe_3O_4NPs and Fe_3O_4@SiO_2-NH_2NPs in Figure S1a-i,ii did not show any peak in the investigated wavelength (300−800). The UV−vis spectrum of Fe_3O_4@SiO_2-NH_2NPs in Figure S1a-ii was similar and overlapped with that of Fe_3O_4@SiO_2NPs shown in Figure 1a-i. For simplicity, we only showed the UV−vis spectra of Fe_3O_4@SiO_2NPs in Figure 1a-i. The absorption spectrum of the AuNPs in Figure 1a-ii showed surface plasmon resonance (SPR) at 514 nm, and this is characteristic of small spherical nanoparticles with size less than 10 nm.[40] The absorption spectrum of the Fe_3O_4@SiO-NH_2-AuNPs in Figure 1a-iii exhibited a weak SPR band at 527 nm and confirmed the adsorption AuNPs onto Fe_3O_4@SiO_2NPs to form Fe_3O_4@SiO_2-NH_2-AuNPs. The AuNP peak at 527 nm disappeared after the reduction of Pd^{2+} onto Fe_3O_4@SiO-NH_2-AuNPs to

DOI: 10.1021/acsami.9b15123
ACS Appl. Mater. Interfaces 2020, 12, 1973−1987

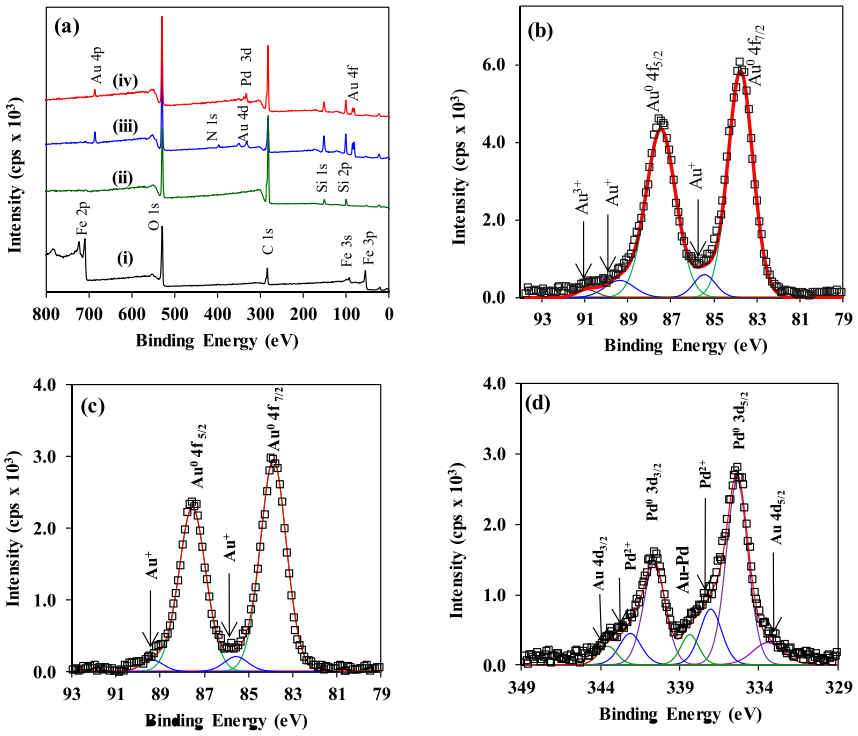

Figure 3. (a) XPS survey spectra of (i) Fe_3O_4, (ii) Fe_3O_4@SiO_2NPs, (iii) Fe_3O_4@SiO_2-NH_2-AuNPs, and (iv) Fe_3O_4@SiO_2-NH_2-Au@PdNPs. High resolution core level Au 4f spectra of (b) Fe_3O_4@SiO_2-NH_2-AuNPs, (c) Fe_3O_4@SiO_2-NH_2-Au@PdNPs, and (d) Pd 3d spectrum of Fe_3O_4@SiO_2-NH_2-Au@PdNPs.

form Fe_3O_4@SiO-NH_2-Au@PdNPs, Figure 1a-iv. The masking of the AuNPs SPR confirms the formation of the Pd shell on the deposited AuNPs and is consistent with the formation of bimetallic (Au@PdNPs) with Au core and Pd shell.[41]

The DLS results, in Figure 1b, clearly showed the changes in ζ-potential for the synthesized nanoparticles measured in pH 7.0. The ζ-potential values indicate that the Fe_3O_4 (−21.0 mV) and Fe_3O_4@SiO_2NPs (−27.2 mV) were negatively charged at neutral pH 7.0 with an isoelectric point at pH 4.0. The negative ζ-potential values were ascribed to the presence of the surface hydroxyl (−OH) and silanol (Si−OH) groups. After the modification of the Fe_3O_4@SiO_2NPs with APTES, the ζ-potential at neutral pH increased from −27.2 to +31.4 mV and the isoelectric point shifted to pH 10. The changes in the value of the ζ-potential to a more positive value (+31.4 mV) confirmed the grafting of APTES to the Fe_3O_4@SiO_2NPs forming Fe_3O_4@SiO_2-NH_2NPs with terminal amine groups. However, the deposition of the AuNPs and Pd shell to form Fe_3O_4@SiO_2-NH_2-Au@PdNPs resulted in a shift of the ζ-potential to more negative values to −10.2 mV for Fe_3O_4@SiO_2-NH_2-AuNPs and −23.2 mV for Fe_3O_4@SiO_2-NH_2-Au@PdNPs. The potential changes after the deposition of the bimetallic Au@Pd were attributed to the N−Au and Pd shell formation. The negative charge is due to the borohydride (BH_4^-) anions capping the gold and palladium shell.

Figure 1c shows the X-ray diffractograms of (i) Fe_3O_4, (ii) Fe_3O_4@SiO_2-NH_2NPs, (iii) Fe_3O_4@SiO_2-NH_2-AuNPs, and (iv) Fe_3O_4@SiO_2-NH_2-Au@PdNPs. The XRD pattern of the Fe_3O_4 in Figure 1c-i showed six characteristic diffraction peaks (2θ) at 30.2, 35.8, 43.4, 54.2, 57.8, and 62.8° corresponding to the (220), (311), (400), (422), (511), and (440) crystal planes of pure magnetite (Fe_3O_4) with a cubic spinel structure (JCPDS No: 03-065-3107). The high crystallinity of the Fe_3O_4 was evident from the sharp diffraction pattern peaks. The XRD pattern of Fe_3O_4@SiO_2NPs in Figure S1b was similar to that of Fe_3O_4@SiO_2-NH_2NPs. We have shown the XRD pattern of Fe_3O_4@SiO_2-NH_2NPs in Figure 1c-ii as representative of the two samples. The XRD pattern of the Fe_3O_4@SiO_2-NH_2NPs in Figure 1c-ii showed that the crystallinity of the Fe_3O_4 core was retained after the silica coating. The broad diffraction band at $2\theta < 20.1°$ corresponds to the amorphous nature of the silica shell and confirms the coating of the magnetic core with a silica shell. The XRD pattern of Fe_3O_4@SiO_2-NH_2-AuNPs and Fe_3O_4@SiO_2-NH_2-Au@PdNPs in Figure 1c-iii,iv, respectively, showed additional diffraction peaks (2θ) at 38.5, 68.05, and 77.8°. These were indexed for the Miller Indices (111), (220), and (311) planes of the face-centered cubic structure of the crystalline Au core even after coating with Pd shell. After the deposition of Pd shell for the formation of Fe_3O_4@SiO_2-NH_2-Au@PdNPs, the intensity of the Au(111) peak in Figure 1c-iv decreased. The attenuation of the AuNP peak has previously been observed in the XRD pattern of core−shell nanoparticles.[42,43]

A transmission electron microscope (TEM) was used to confirm the detailed morphology and nanoscale dimensions of the nanoparticles. Figure 2 shows the TEM micrograph and corresponding size distribution histograms of (a) Fe_3O_4NPs, (b) Fe_3O_4@SiO_2-NH_2NPs, and (c) Fe_3O_4@SiO_2-NH_2-Au@PdNPs. The TEM micrograph, in Figure 2a, of Fe_3O_4, exhibited spherical monodispersed nanoparticles with an average size distribution of 15.0 ± 1.8 nm. The TEM micrograph of Fe_3O_4NPs coated with silica shell, Fe_3O_4@SiO_2NPs (data not shown), was similar to that of the Fe_3O_4@SiO_2-NH_2NPs shown in Figure 2b. The Fe_3O_4 core was visible with a single Fe_3O_4NP within a silica shell, in Figure 2b. The TEM also showed core−shell nanoparticles agglomerated and

DOI: 10.1021/acsami.9b15123
ACS Appl. Mater. Interfaces 2020, 12, 1973−1987

overlapping with each other. The Fe_3O_4@SiO_2-NH_2NPs have an average size of 42.5 ± 13.9 nm. The magnetic separation also afforded only the silica-coated nanoparticles with Fe_3O_4 core. The growth in nanoparticle sizes from 15.0 ± 1.8 nm for Fe_3O_4NPs to 42.5 ± 13.9 nm Fe_3O_4@SiO_2-NH_2NPs confirmed the formation of the silica shell. The TEM images of Fe_3O_4@SiO_2-NH_2-Au@PdNPs in Figure 2c showed agglomeration with some distinct deposited nanoparticles smaller in sizes to the Fe_3O_4NPs. The TEM image of Fe_3O_4@SiO_2-NH_2-Au@PdNPs in Figure 2c shows the presence of the dispersed Au@PdNPs as dark spots. The size distribution of the Au@PdNPs was 7.8 ± 3.9 nm. The size of AuNPs grew from 3.5 to 7.8 ± 3.9 nm. The growth of the Au@PdNPs was due to the formation of Pd shell encapsulating 3.5 nm AuNPs. The TEM images confirmed the successful deposition of Au@PdNPs and formation of Fe_3O_4@SiO_2-NH_2-Au@PdNPs. The sizes of the nanoparticles was measured using the TEM, as shown in the Figure S2.

Furthermore, the elemental composition of each sample was investigated using energy dispersive X-ray spectroscopy (EDS). Figure S3 (SI) shows the EDS spectra of (a) Fe_3O_4, (b) Fe_3O_4@SiO_2-NH_2NPs, and (c) Fe_3O_4@SiO_2-NH_2-AuNPs and Fe_3O_4@SiO_2-NH_2-Au@PdNPs. The various elements were observed corresponding to the nanoparticles investigated. We noted the presence of Fe, C, and O for the Fe_3O_4 (oleate); in addition, Si peak was observed at Fe_3O_4@SiO_2NPs; Au and Pd peaks were observed at Fe_3O_4@SiO_2-NH_2-AuNPs and Fe_3O_4@SiO_2-NH_2-Au@PdNPs, respectively. The quantitative analysis of the elemental composition was observed and are summarized in Table S1. The Fe peak was observed even after coating with a silica shell. The X-rays of the EDS have a high depth resolution that penetrates deep into the core of the nanoparticles. The decrease in Fe peak and an increase in O peak was observed after each modification with a silica shell. The Fe peak decreased further as the modification continued. The O peak increased after APTES-AuNPs coat and decreased after Au@PdNP formation. The Si peak was observed after the silica coating and persisted even after decorating the Fe_3O_4@SiO_2-NH_2NPs with Au@PdNPs. The Au peak was observed after AuNPs decoration. It decreased after Pd shell for Fe_3O_4@SiO_2-NH_2-Au@PdNPs. The EDS gives a rough estimate of the elemental composition. X-ray photoelectron spectroscopy (XPS) was used to further confirm the elemental composition and the oxidation states of the elements present within each sample. XPS is a sensitive quantitative analytical technique.

Figure 3 shows the (a) XPS survey spectra, high-resolution Au 4f core-level spectra of (b) Fe_3O_4@SiO_2-NH_2-AuNPs and (c) Fe_3O_4@SiO_2-NH_2-Au@PdNPs, and (d) high-resolution Pd 3d core level spectrum of Fe_3O_4@SiO_2-NH_2-Au@PdNPs. The survey spectra were for (i) Fe_3O_4, (ii) Fe_3O_4@SiO_2NPs, (iii) Fe_3O_4@SiO_2-NH_2-AuNPs, and (iv) Fe_3O_4@SiO_2-NH_2-Au@PdNPs. The survey spectrum of Fe_3O_4 in Figure 3a-i shows elements present in the sample at 54 eV (Fe 3p), 92 eV (Fe 3s), 283 eV (C 1s), 531 eV (O 1s), and 711−722 eV (Fe 2p). The elemental composition was 31.3% (Fe 2p), 30.2% (C 1s), and 38.5% (O 1s). The ratio of Fe 2p to O 1s was 3 to 4, confirming that the Fe_3O_4 was synthesized as confirmed by the XRD results above. The C 1s was due to the hydrocarbon backbone of the oleate capping agent. The Fe peaks (Fe 3p, Fe 3s, and Fe 2p) disappeared after coating the Fe_3O_4 with a silica shell to form Fe_3O_4@SiO_2NPs in Figure 3a-ii. The additional two peaks assigned to the binding energies of Si 2p (100 eV) and Si 2s (152 eV) were observed, confirming the silica shell. Compared with the EDS analysis, XPS is a surface technique and X-rays have 10 nm depth resolution.[44] This resulted in the attenuation of the Fe peaks by the silica shell. The average size distribution of the Fe_3O_4NPs was 15.0 ± 1.8 nm, and after the silica shell the average size was 42.5 ± 13.9 nm. The average shell size was ∼14 nm and hence resulted in the attenuation of the Fe peaks. The survey spectrum of Fe_3O_4@SiO_2-NH_2-AuNPs in Figure 3a-iii showed additional peaks at Au 4f (82 eV), Au 4d (331 eV), Au 4p (686 eV), and N 1s (392 eV). The presence of the N 1s peaks confirmed the successful modification of Fe_3O_4@SiO_2NPs with APTES to form Fe_3O_4@SiO_2-NH_2NPs. The Au peaks (Au 4f, Au 4d, and Au 4p) confirm the successful deposition of AuNPs to form Fe_3O_4@SiO_2-NH_2-AuNPs. Also, the appearance of the Pd 3d peak at 333.5 eV in Figure 3a-iv confirmed the deposition of Pd to form Fe_3O_4@SiO_2-NH_2-Au@PdNPs. The elemental composition is summarized in Table S2.

The high-resolution core-level XPS spectra of Au 4f and Pd 3d in the Fe_3O_4@SiO_2-NH_2-AuNPs and Fe_3O_4@SiO_2-NH_2-Au@PdNPs were analyzed to determine the oxidation state of Au and Pd. The deconvoluted Au 4f high-resolution spectrum of Fe_3O_4@SiO_2-NH_2-AuNPs in Figure 3b was fitted into five components with two pairs of doublets ascribed to the Au $4f_{7/2}$ and Au $4f_{5/2}$ with split spin−orbit coupling (Δ) of 3.7 eV. The most prominent peaks at 83.6 eV (48.9%) and 87.3 eV (41.9%) were assigned to Au $4f_{7/2}$ and Au $4f_{5/2}$ of metallic gold (Au^0). The value of the Au^0 binding energies in Fe_3O_4@SiO_2-NH_2-AuNPs was 0.4 eV lower than 84.0 eV for Au $4f_{7/2}$ and 87.7 eV for Au $4f_{5/2}$ of pristine gold nanoparticle.[45,46] The peaks at 85.5 eV (3.54%) and 89.4 eV (4.4%) were assigned to Au^+ oxidation state. The Au^0 (at 83.6 eV) and Au^+ (at 85.5 eV) are 1.9 eV apart, which is approximately 2.0 eV.[47] The deposited AuNPs bonded to the APTES ($-NH_2$) and BH_4^- capping agent, resulting in the Au^+ oxidation state. The deconvolution of the Au 4f spectrum of Fe_3O_4@SiO_2-NH_2-Au@PdNPs in Figure 3c was fitted into four components. The binding energies of Au $4f_{7/2}$ and Au $4f_{5/2}$ increased from 83.6 to 87.3 eV in Fe_3O_4@SiO_2-NH_2-AuNPs to 84.0 eV (52.1%) and 87.8 eV (41.0%) for Au $4f_{7/2}$ and Au $4f_{5/2}$; respectively for Fe_3O_4@SiO_2-NH_2-Au@PdNPs. The increase in binding energy is consistent with previous studies on supported bimetallic Au−Pd nanoparticles.[45,48,49] The shift of the Au 4f peak in Fe_3O_4@SiO_2-NH_2-Au@PdNPs to higher binding energy values suggested that there exists an electron transfer interaction between the Au core and the Pd shell. Electrons flow from the Au to the d-orbital of the Pd due to charge complexation between Au and Pd.[50,51] The Au gains sp-type charges and loses d-charge.

The XPS analysis reveals that there was strong metal-to-metal interaction (Au−Pd) between the Au core and the Pd shell. The deconvoluted spectrum of Pd 3d in Figure 3d was fitted into seven components. The binding energy values of Pd 3d overlapped with Au 4d for the Fe_3O_4@SiO_2-NH_2-Au@PdNPs. The main components at binding energies of 335.1 eV (41.5%) and 340.2 (22.7%) were assigned to the Pd $3d_{5/2}$ and Pd $3d_{3/2}$, respectively. The split spin-orbit coupling (Δ) between Pd $3d_{5/2}$ and Pd $3d_{3/2}$ was 5.2 eV, which is close to previously reported values.[52] Pd $3d_{5/2}$ and Pd $3d_{3/2}$ were attributed to PdNPs with an oxidation state of zero for Pd^0 and Pd^{2+}. The binding energies of Pd $3d_{5/2}$ and Pd $3d_{3/2}$ shifted to lower energy by 0.7 eV relative to the binding energies of pure metallic Pd nanoparticles.[53] The lowered binding energy of the Pd 3d further confirms that Pd formed a shell around the

DOI: 10.1021/acsami.9b15123
ACS Appl. Mater. Interfaces 2020, 12, 1973−1987

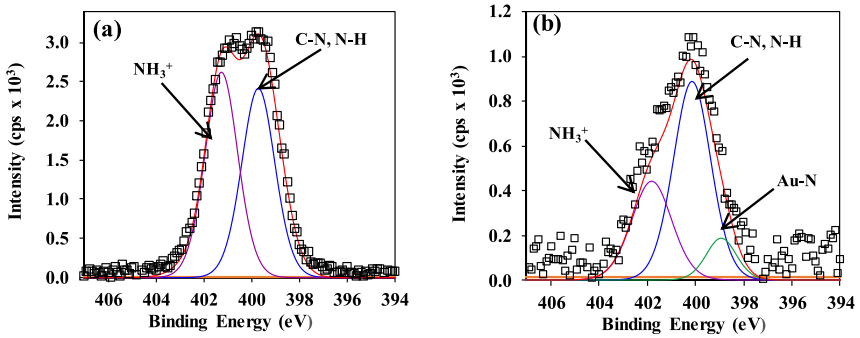

Figure 4. High-resolution N 1s core-level spectra of (a) Fe_3O_4@SiO_2-NH_2NPs and (b) Fe_3O_4@SiO_2-NH_2-AuNPs (Au@PdNPs).

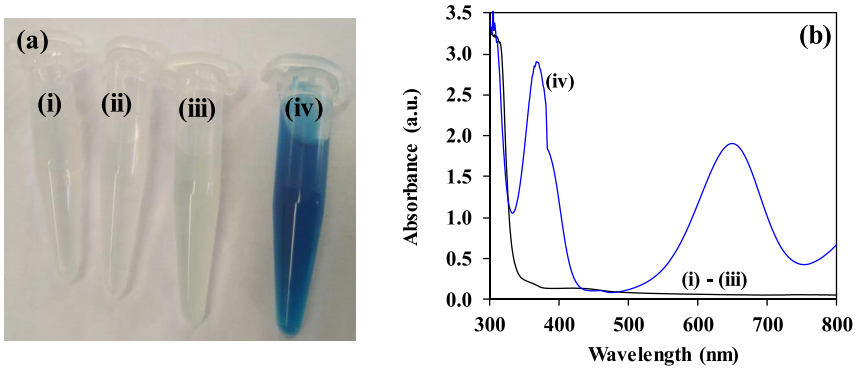

Figure 5. (a) Images and (b) UV−vis absorption spectra of (i) 6.67 mM H_2O_2 + 0.42 mM TMB, (ii) 6.67 mM H_2O_2 + 1.33 μg L^{-1} Fe_3O_4@SiO_2-NH_2-Au@PdNPs, (iii) 0.42 mM TMB + 1.33 μg L^{-1} Fe_3O_4@SiO_2-NH_2-Au@PdNPs, and (iv) 6.67 mM H_2O_2 + 0.42 mM TMB + 1.33 μg L^{-1} Fe_3O_4@SiO_2-NH_2-Au@PdNPs.

AuNPs core in the Fe_3O_4@SiO_2-NH_2-Au@PdNPs. The additional doublet located at 336.8 eV (12.7%) and 342.5 (7.2%) was attributed to the $Pd^{II}3d_{5/2}$ and $Pd^{II}3d_{3/2}$ of PdO, respectively. The Au 4d peak at 332.9 (6.8%) with its split spin-orbit couple at 344.0 (3.5%) were characteristics of the Au $4d_{5/2}$ and Au $4d_{3/2}$ with Δ of 11.1 eV. A similar decrease in binding energies was reported for various metallic nanoparticles.[53−56] In addition to the high resolution of Au 4f and Pd 3d, the N 1s was also investigated. Figure 4 shows the high-resolution N 1s core-level spectra of (a) Fe_3O_4@SiO_2-NH_2NPs and Fe_3O_4@SiO_2-NH_2-AuNPs. In Figure 4a, the N 1s spectrum was deconvoluted into two peaks at 399.5 eV (N−H, C−N) and 401.5 eV ($-NH_3^+$). Both peaks were due to the propylamine (C−N and N−H) functional group from the APTES. After the adsorption of Au@PdNPs onto Fe_3O_4@SiO_2-NH_2NPs, in Figure 4b, the N 1s high resolution core level spectrum was deconvoluted, and three peaks were obtained at 398.7 eV (Au−N), 400.3 eV (N−H, C−N), and 402.2 eV ($-NH_3^+$). It was interesting to obtain the synthesized peak at low binding energy (398.7 eV) corresponding to N−AuNPs and same for N−Au@PdNPs. The data confirms the formation of Fe_3O_4@SiO_2-NH_2-Au@PdNPs.

Peroxidase-Like Activity of Fe_3O_4@SiO_2-NH_2-Au@PdNPs. The peroxidase-like activity of the Fe_3O_4@SiO_2-NH_2-Au@PdNPs was investigated using TMB as chromogenic substrates in the presence of H_2O_2. The detailed procedure in the Experimental Section (in the SI) was carried out for the peroxidase-like activity of Fe_3O_4@SiO_2-NH_2-Au@PdNPs. Figure 5 shows the (a) images and (b) UV−vis absorption spectra in an acetate buffer (pH 5.0) solution containing (i) 6.67 mM H_2O_2 + 0.42 mM TMB, (ii) 6.67 mM H_2O_2 + 1.33 μg L^{-1} Fe_3O_4@SiO_2-NH_2-Au@PdNPs, (iii) 0.42 mM TMB + 1.33 μg L^{-1} Fe_3O_4@SiO_2-NH_2-Au@PdNPs, and (iv) 6.67 mM H_2O_2 + 0.42 mM TMB + 1.33 μg L^{-1} Fe_3O_4@SiO_2-NH_2-Au@PdNPs. The image in Figure 5a-iv shows that a deep blue color developed in the presence of H_2O_2 + TMB + Fe_3O_4@SiO_2-NH_2-Au@PdNPs and due to the oxidation of 3,3′,5,5-tetramethylbenzidine (TMB) to 3,3′,5,5′-tetramethylbenzodiimine (TMBDI). The other combinations in Figure 5a-i−iii showed a clear solution. The UV−vis absorption spectrum in Figure 5b-iv showed that the TMBDI product had maximum absorption at 370 and 652 nm. This confirmed that Fe_3O_4@SiO_2-NH_2-Au@PdNPs possess intrinsic peroxidase-like activity. Similar results were observed when horseradish peroxidase (HRP) was used for the oxidation of TMB to form TMBDI in the presence of H_2O_2. The clear solutions in Figure 5a-i−iii did not produce absorption in the wavelength measured. This experiment showed that TMB + H_2O_2 + Fe_3O_4@SiO_2-NH_2-Au@PdNPs are required for the efficient oxidation of TMB to TMBDI. The color development of TMBDI was monitored with time, and an increase in absorption was observed up to 28 min, in Figure S4a-iv. Other nanomaterials, in Figure S4a-i for Fe_3O_4@SiO_2-NH_2NPs, (ii) Fe_3O_4@SiO_2-NH_2-AuNPs, and (iii) Fe_3O_4@ SiO_2-NH_2-PdNPs also exhibited an increase in absorption at 652 nm confirming their peroxidase-like activity. The Fe_3O_4@SiO_2-NH_2-Au@PdNPs showed 70% enhancement in the absorption and formation of TMBDI better than Fe_3O_4@SiO_2-NH_2NPs with AuNPs and PdNPs alone. The silica shell-coated Fe_3O_4@SiO_2-NH_2NPs, exhibited a minimal increase in the absorption at 652 nm compared with metal-coated nanomaterials. The oxidation of TMB occurred on the metal nanoparticle and only in the presence of H_2O_2, which undergoes reduction and oxidize TMB to TMBDI. The leaching test in acid-treated nanoparticles was studied to

DOI: 10.1021/acsami.9b15123
ACS Appl. Mater. Interfaces 2020, 12, 1973−1987

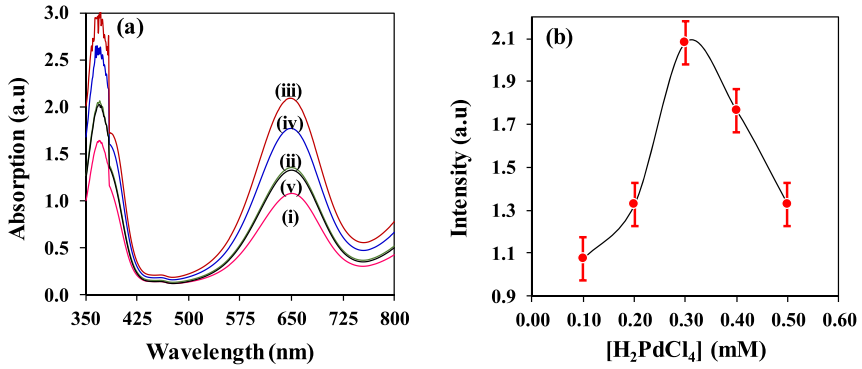

Figure 6. (a) UV−vis absorption spectra of peroxidase-like activity in 6.67 mM H_2O_2 + 0.42 mM TMB with 1.33 μg mL^{-1} of (i) Fe_3O_4@SiO_2-NH_2-Au@$Pd_{0.10}$NPs, (ii) Fe_3O_4@SiO_2-NH_2-Au@$Pd_{0.20}$NPs, (iii) Fe_3O_4@SiO_2-NH_2-Au@$Pd_{0.30}$NPs, (iv) Fe_3O_4@SiO_2-NH_2-Au@$Pd_{0.40}$ NPs, and (v) Fe_3O_4@SiO_2-NH_2-Au@$Pd_{0.50}$NPs, and (b) plot of absorption intensity versus [H_2PdCl_4] concentrations to form Pd shell.

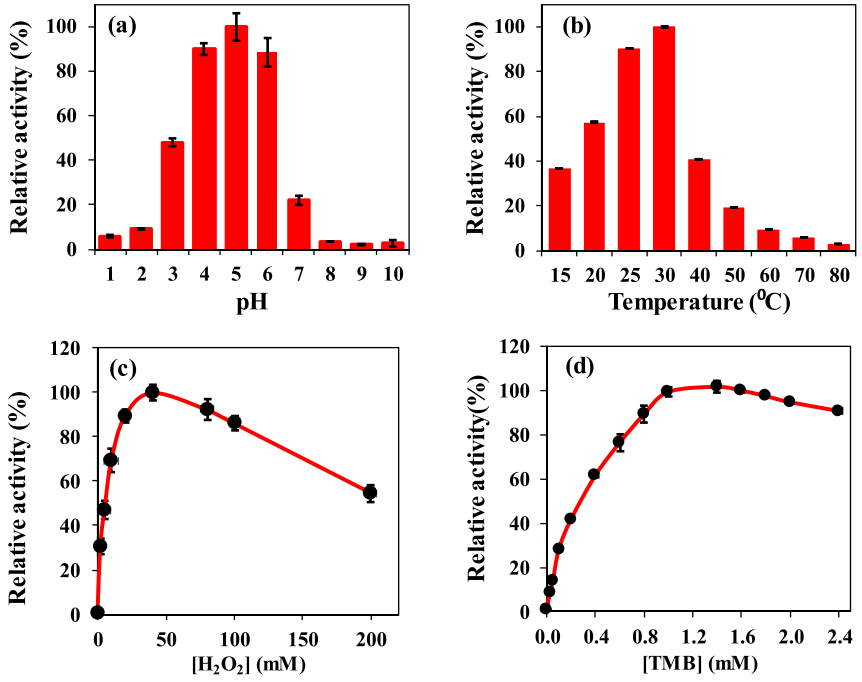

Figure 7. Effect of (a) pH, (b) temperature, (c) concentrations of H_2O_2, and (d) concentration of TMB on the peroxidase-like activity of Fe_3O_4@SiO_2-NH_2-Au@$Pd_{0.30}$NPs.

investigate whether the peroxidase-like activity originates from an intact Fe_3O_4@SiO_2-NH_2-Au@PdNPs or leached metal ions (Fe^{3+}, Pd^{2+}, and Au^{3+}). The Fe_3O_4@SiO_2-NH_2-Au@PdNPs were incubated in the pH 4.5 sodium acetate buffer for 3 h. The intact Fe_3O_4@SiO_2-NH_2-Au@PdNPs were collected by magnetic separation. The collected nanaoparticles and the supernatant were each evaluated for their peroxidase activity. Figure S4b shows the UV−vis absorption spectra of TMBDI catalyzed by (i) supernatant solution and (ii) recovered Fe_3O_4@SiO_2-NH_2-Au@PdNPs. The UV−vis spectrum in Figure S4b-i for the supernatant showed negligible absorption peaks at 370 and 652 nm when compared with the strong absorption peaks for Fe_3O_4@SiO_2-NH_2-Au@PdNPs, in Figure 2b-ii. This confirmed that the peroxidase-like activity was due to the intact Fe_3O_4@SiO_2-NH_2-Au@PdNPs. Since, Fe_3O_4@SiO_2-NH_2-Au@PdNPs showed better peroxidase-like activity, they were investigated further. Different batches of Fe_3O_4@SiO_2-NH_2-Au@PdNPs, in Figure S4c, showed reproducible TMBDI color development with relative standard deviation (% RSD, n = 3) less than 3.5%.

Effect of Pd-Shell Thickness on Peroxidase-Like Activity of Fe_3O_4@SiO_2-NH_2-Au@PdNPs. The Fe_3O_4@SiO_2-NH_2-Au@PdNPs were synthesized from the same batch of Fe_3O_4@SiO_2-NH_2-AuNPs by adding different concentrations of H_2PdCl_4 ranging from 0.10 to 0.50 mM and the same concentration of $NaBH_4$. The synthesized nanoparticles were represented as Fe_3O_4@SiO_2-NH_2-Au@$Pd_{0.10}$NPs, Fe_3O_4@SiO_2-NH_2-Au@$Pd_{0.20}$NPs, Fe_3O_4@SiO_2-NH_2-Au@$Pd_{0.30}$NPs, Fe_3O_4@SiO_2-NH_2-Au@$Pd_{0.40}$NPs, and Fe_3O_4@SiO_2-Au@$Pd_{0.50}$NPs for 0.10, 0.20, 0.30, 0.40, and 0.50 mM H_2PdCl_4 concentrations, respectively. Figure 6a shows the UV−vis absorption spectra of peroxidase-like activity in 6.67 mM H_2O_2 + 0.42 mM TMB with 1.33 μg L^{-1} of (i) Fe_3O_4@SiO_2-NH_2-Au@$Pd_{0.10}$NPs, (ii) Fe_3O_4@SiO_2-NH_2-Au@$Pd_{0.20}$NPs, (iii) Fe_3O_4@SiO_2-NH_2-Au@$Pd_{0.30}$NPs, (iv) Fe_3O_4@SiO_2-NH_2-Au@$Pd_{0.40}$ NPs, and (v) Fe_3O_4@SiO_2-NH_2-Au@$Pd_{0.50}$NPs, and (b) plot of absorption intensity versus [H_2PdCl_4]

DOI: 10.1021/acsami.9b15123
ACS Appl. Mater. Interfaces 2020, 12, 1973−1987

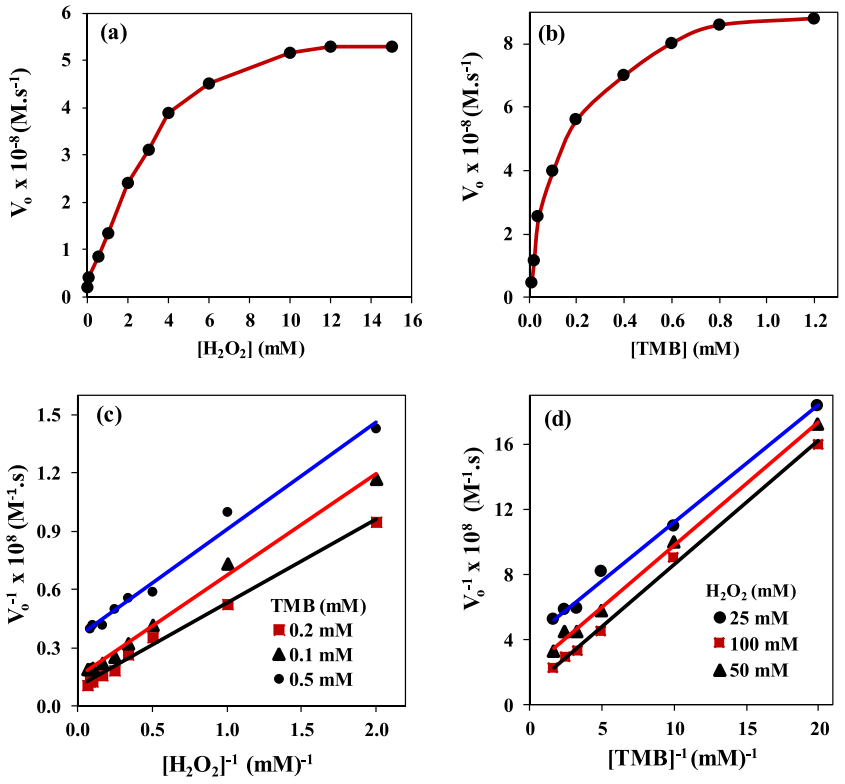

Figure 8. (a) Plot of initial velocity versus [H_2O_2] at a fixed [TMB], (b) plot of initial velocity versus [TMB] at a fixed [H_2O_2], and corresponding double reciprocal plot of initial velocity versus (c) [H_2O_2] at different fixed [TMB], and (d) [TMB] at different fixed [H_2O_2].

concentrations of the Pd shell. The absorption intensity increased with increasing concentration of H_2PdCl_4 up to 0.30 mM and decreased afterward. The increase in the absorption intensity was attributed to an increase in Pd shell thickness as the concentration increased, allowing the efficient electron transfer to occur. After 0.30 mM, the increase in a Pd-shell could not allow for the efficient electron transfer from the AuNPs to Pd-shell and hence the decreased in intensity. Therefore, 0.30 mM of H_2PdCl_4 afforded an optimum Pd-shell for efficient electron transfer and was the optimum concentration chosen for Pd-shell deposition in Fe_3O_4@SiO_2-NH_2-Au@$Pd_{0.30}$NPs. Figure 6b shows that the Fe_3O_4@SiO_2-NH_2-Au@$Pd_{0.30}$NPs had the highest absorption intensity and is the optimum concentration of H_2PdCl_4 for a Pd shell. Therefore, Fe_3O_4@SiO_2-NH_2-Au@$Pd_{0.30}$NPs was used for subsequent studies. It was also interesting to observe that the XRD patterns of increasing concentration of H_2PdCl_4 resulted in the attenuation of the Au(111) peak in the XRD pattern in Figure S5a. The XRD pattern in Figure S5a shows that Pd shell grew as the concentration of H_2PdCl_4 increased. The attenuation of the intense Au(111) peak with increasing concentrations of H_2PdCl_4 suggests that the PdNPs were deposited on the AuNPs of Fe_3O_4@SiO_2-NH_2-AuNPs that acted as nucleation sites. PdNPs can also be deposited onto the vacant Fe_3O_4@SiO_2-NH_2NPs.

Effect of Conditions on Peroxidase-Like Activity of Fe_3O_4@SiO_2-NH_2-Au@$Pd_{0.30}$NPs. The effect of pH, temperature, the concentration of TMB and H_2O_2 on the peroxidase-like activity of the Fe_3O_4@SiO_2-NH_2-Au@$Pd_{0.30}$NPs was evaluated. Figure 7 shows the effect of (a) pH (1−10), (b) temperature (15−80 °C), (c) [H_2O_2] (0−100 mM), and (d) [TMB] (0.0−2.4 mM) on the Fe_3O_4@SiO_2-NH_2-Au@$Pd_{0.30}$NPs peroxidase-like activity. In Figure 7a, the pH 5.0 showed the maximum activity as measured by the highest absorption at 625 nm. The other pH 4.0 and 6.0 showed comparable activity to pH 5.0. A drastic decrease was observed at high pH > 8.0, and due to the instability of H_2O_2, at alkaline pH. The wider pH range has been reported for some other peroxidase-like nanozymes[5,13,57] and therefore would be beneficial for sensing applications. In Figure 7b, the effect of temperature on the peroxidase-like activity was also investigated and increased up to 30 °C and drastically decreased afterward. Thus, 30 °C is the optimum temperature for the Fe_3O_4@SiO_2-NH_2-Au@$Pd_{0.30}$NPs. The effect of concentrations of H_2O_2 and TMB was studied in Figure 7c,d. An increase in peroxidase-like activity for H_2O_2 concentrations up to 40.0 mM and for TMB concentrations up to 0.80 mM was observed, and these concentrations were taken as optimum. A decrease in the relative activity was observed at higher concentrations of H_2O_2 (>40.0 mM) in the reaction system. At higher concentrations of H_2O_2 and TMB, there is a competition for single catalytic sites on the Fe_3O_4@SiO_2-NH_2-Au@$Pd_{0.30}$NPs, as a result no catalysis occured. The competition for single catalytic sites results in the decrease catalytic activity. This phenomenon is similar to that observed for HRP and some other peroxidase-like nanozymes.[58,59] Similarly, the relative activity increases gradually with increasing TMB concentration and attained a plateau at higher TMB concentrations.

Enzyme-Like Kinetics of Fe_3O_4@SiO_2-NH_2-Au@$Pd_{0.30}$NPs Peroxidase-Like Activity. The steady-state kinetics of TMB oxidation using Fe_3O_4@SiO_2-NH_2-Au@$Pd_{0.30}$NPs was studied by changing the concentration of either TMB or H_2O_2 while keeping the concentrations of other reagents constant. A series of initial rates (V_o) of TMB oxidation were calculated from the time-dependent absorption

DOI: 10.1021/acsami.9b15123
ACS Appl. Mater. Interfaces 2020, 12, 1973−1987

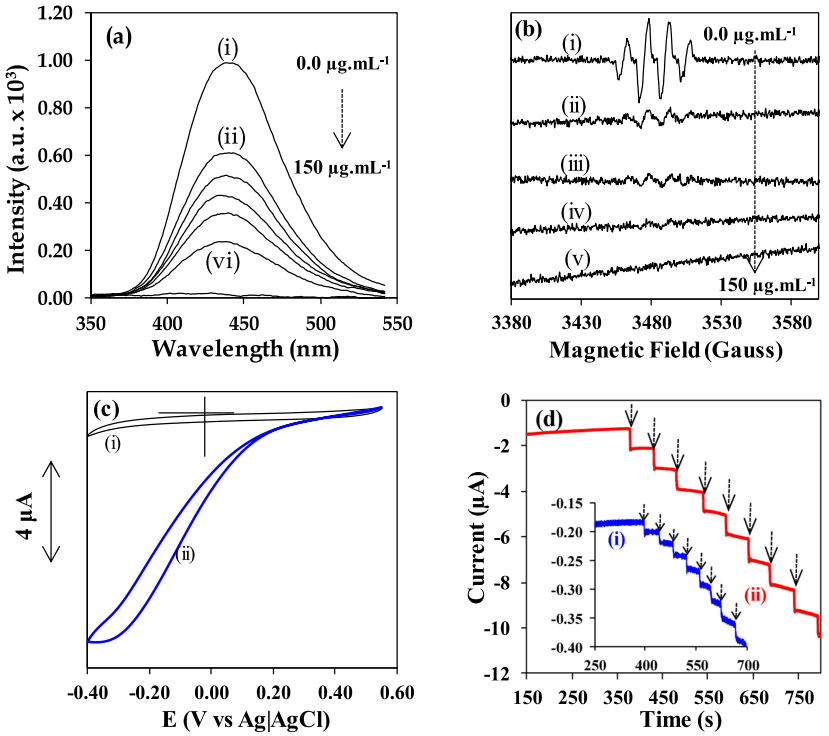

Figure 9. (a) Fluorescence spectra of the interaction of HTA and (b) EPR signal or the interaction of DMPO as $^{\bullet}OH$ spin trap after introducing different concentrations of Fe_3O_4@SiO_2-NH_2-Au@$Pd_{0.30}$NPs ranging from (i) 0.0 μg mL^{-1} to (vi) 150.0 μg mL^{-1}. (c) Cyclic voltammograms of GCE-Fe_3O_4@SiO_2-NH_2-Au@$Pd_{0.30}$NPs electrode in 0.10 M sodium acetate buffer (pH 5.0) in the (i) absence, (ii) and presence of 6.67 mM H_2O_2, and (d) amperometric response at increasing [H_2O_2].

value at 652 nm. The absorption values were converted to concentrations using the molar absorption coefficient of oxidized TMB products ($\sum_{TMBox}$ = 39 000 M^{-1} cm^{-1} at 652 nm) using eq 1.[57]

$$[TMB_{ox}] = \frac{A}{\sum_{[TMB_{ox}]} \times L} \quad (1)$$

The typical Michaelis–Menten curves were obtained by plotting the initial rates against concentrations of TMB or H_2O_2. The Michaelis–Menten parameters (Michaelis–Menten constant, K_m and maximum velocity, V_{max}) for H_2O_2 and TMB were obtained from the Lineweaver–Burk or double reciprocal plot $\left(\frac{1}{V_0} \text{ vs } \frac{1}{[S]}\right)$ using eq 2.

$$\frac{1}{V_0} = \frac{K_m}{V_{max}[S]} + \frac{1}{V_{max}} \quad (2)$$

Figure 8a,b shows that the peroxidase-like activity of Fe_3O_4@SiO_2-NH_2-Au@$Pd_{0.30}$ NPs follows a typical Michaelis–Menten enzyme behavior. The double reciprocal of the initial rate (V_o) versus the substrate concentrations in Figure 8c,d gave an excellent linear relationship. Equations 3 and 4 shows the linear regression equations

$$\frac{1}{V_o} = 1.15 \times 10^6 \frac{1}{[TMB]} + 1.12 \times 10^7, \; R^2 = 0.994 \quad (3)$$

$$\frac{1}{V_0} = 5.25 \times 10^6 \frac{1}{[H_2O_2]} + 1.48 \times 10^7, \; R^2 = 0.994 \quad (4)$$

The K_m and V_{max} values were calculated from the slope and intercepts of the corresponding linear graphs. The result of the calculated parameters and the comparison with other nanozymes and HRP are summarized in Table S3. The K_m values of 0.35 and 0.09 mM were obtained for H_2O_2 and TMB, respectively. The K_m values for both substrates were lower than that of HRP,[11,60] indicating that Fe_3O_4@SiO_2-NH_2-Au@$Pd_{0.30}$NPs showed high affinity for TMB and H_2O_2 than HRP. The higher affinity for both substrates is attributed to the large surface area and numerous active catalytic sites on the Fe_3O_4@SiO_2-NH_2-Au@$Pd_{0.30}$NPs. The V_{max} of Fe_3O_4@SiO_2-NH_2-Au@$Pd_{0.30}$NPs with TMB as substrate (8.65×10^{-8} M s^{-1}) and H_2O_2 as the substrate (6.78×10^{-8} M s^{-1}) was comparable to that of HRP (8.70×10^{-8} M s^{-1}).[11] Also, the K_m of Fe_3O_4@SiO_2-NH_2-Au@$Pd_{0.30}$NPs with the TMB substrate (0.090 mM) was lower than that of FePt-Au hybrid (0.46 mM),[61] Fe-MiL-88-NH_2 (0.28 mM),[62] $ZnFe_2O_4$ MNPs (0.85 mM),[63] and CuO–Au nanoalloys (3.54 mM)[19] and comparable to that of CuONPs (0.010 mM)[64] and Pt/Ni@NGT (0.019 mM).[65] Fe_3O_4@SiO_2-NH_2-Au@$Pd_{0.30}$NPs have a higher affinity for TMB and H_2O_2 compared with the previously reported nanozymes. The kinetic parameters showed that Fe_3O_4@SiO_2-NH_2-Au@$Pd_{0.30}$NPs possessed excellent peroxidase-like activity. The double reciprocal plots of TMB oxidation against the H_2O_2 at different fixed TMB concentrations afforded a set of linear and parallel lines, Figure 8c,d. This is indicative of the ping-pong π-π mechanism (double displacement mechanism). The Fe_3O_4@SiO_2-NH_2-Au@$Pd_{0.30}$NPs react with the first substrate (H_2O_2) to produce products (H_2O and O_2) and then react with the second substrate, TMB, to produce colored products (TMBDI). This mechanism is similar to that of HRP.[11] The kinetic studies

DOI: 10.1021/acsami.9b15123
ACS Appl. Mater. Interfaces 2020, 12, 1973–1987

Scheme 2. Proposed Peroxidase-Like Mechanism of the Fe_3O_4@SiO_2-NH_2-Au@$Pd_{0.30}$NPs

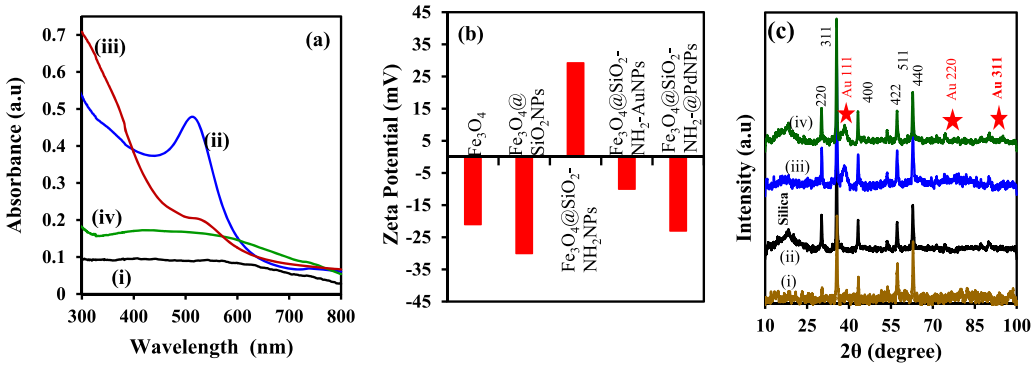

showed that the peroxidase-like activity of Fe_3O_4@SiO_2-NH_2-Au@$Pd_{0.30}$NPs is superior to that of HRP.

Mechanism of Peroxidase-Like Activity of Fe_3O_4@SiO_2-NH_2-Au@$Pd_{0.30}$NPs. The mechanism of the peroxidase-like activity of nanozyme can either proceed via the Fenton-like reaction or the electron transfer process.[66,67] Fenton's reaction pathways involve the decomposition of H_2O_2 to produce reactive oxygen species (ROS) such as hydroxyl ($^{-\bullet}OH$), superoxide ($O_2^{\bullet-}$) and peroxy ($HO_2^{\bullet-}$) radicals. First, the peroxidase-like activity of Fe_3O_4@SiO_2-NH_2-Au@$Pd_{0.30}$NPs via the generation of ROS was investigated using the fluorescence of terephthalic acid and 5,5-dimethyl-1-pyrroline *N*-oxide (DMPO) as radical trapping experiments. Figure 9a shows that the hydroxyterephthalate (HTA) fluorescence and (b) DMPO/$^{\bullet}OH$ electron paramagnetic resonance (EPR) adduct signal decreased with increasing concentrations of Fe_3O_4@SiO_2-NH_2-Au@$Pd_{0.30}$NPs. This indicated that the Fe_3O_4@SiO_2-NH_2-Au@$Pd_{0.30}$NPs did not generate ROS. The electrocatalytic behavior of Fe_3O_4@SiO_2-NH_2-Au@$Pd_{0.30}$NPs was investigated to verify the electron transfer process. The glassy carbon (GC) electrode was modified with the Fe_3O_4@SiO_2-NH_2-Au@$Pd_{0.30}$NPs, the cyclic voltammetric (CV) and amperometric measurements were recorded in the presence and absence of H_2O_2. The CV of the bare GCE electrode is similar, within the studied potential window (+0.60 to −0.40 V), to that of GCE-Fe_3O_4@SiO_2-NH_2-Au@$Pd_{0.30}$NPs in Figure 9c-i. The GCE did not show an increase in the reduction current in the absence and presence of H_2O_2. The Fe_3O_4@SiO_2-NH_2-Au@$Pd_{0.30}$NPs modified GC electrode in Figure 9c-ii showed an electrocatalytic reduction current with a peak at −0.35 V vs AgIAgCl with the addition of H_2O_2 into the acetate buffer (pH 5.0) solution. The electrocatalytic reduction scan showed an early onset at +0.33 V vs AgIAgCl. The chronoamperomograms in Figure 9d are for (i) bare GCE and (ii) GCE-Fe_3O_4@SiO_2-NH_2-Au@$Pd_{0.30}$NPs after each addition of 20 μL of 0.10 mM H_2O_2 (indicated by arrows). The current response of the GCE-Fe_3O_4@SiO_2-NH_2-Au@$Pd_{0.30}$NPs electrode was higher than that of the bare GC electrode. The current response increases steadily with increasing successive addition of 0.10 mM H_2O_2. This showed that Fe_3O_4@SiO_2-NH_2-Au@$Pd_{0.30}$NPs possess excellent electrocatalytic activity and facilitate electron transfer between the electrode (electron donor) and H_2O_2 (electron acceptor). Hence, the peroxidase-like activity of Fe_3O_4@SiO_2-NH_2-Au@$Pd_{0.30}$NPs was attributed to an electron transfer process mimicking HRP-C.[15] The increase in electrocatalytic current for GCE-Fe_3O_4@SiO_2-NH_2-Au@$Pd_{0.30}$NPs was linearly related to the concentration of H_2O_2, as shown in Figure S6a and better than that of bare GCE in Figure S6b in terms of current density. About 98% of the signal was obtained with 1 s of H_2O_2 injection, thus showing a quick response of GCE-Fe_3O_4@SiO_2-NH_2-Au@$Pd_{0.30}$NPs. The limit of detection for GCE-Fe_3O_4@SiO_2-NH_2-Au@$Pd_{0.30}$NPs toward H_2O_2 was calculated using a signal-to-noise ratio of 3 and found to be 4.0 μM with the sensitivity of 0.57 μA μM^{-1}.

The mechanism of peroxidase-like activity of Fe_3O_4@SiO_2-NH_2-Au@$Pd_{0.30}$NPs follows the redox cycles in Scheme 2. The first step involves the reduction of H_2O_2 by Fe_3O_4@SiO_2-NH_2-Au@$Pd_{0.30}$NPs, which is oxidized. This electron transfer process occurs from Au-core to Pd-shell and to the H_2O_2 as an electron acceptor. In the second step, TMB undergoes oxidation to TMBDI (blue color) and reduction of the Pd-shell of the Fe_3O_4@SiO_2-NH_2-Au@$Pd_{0.30}$NPs occurs. The peroxidase-like activity of the Fe_3O_4@SiO_2-NH_2-Au@$Pd_{0.30}$NPs via electron transfer is similar to the HRP-C,[68] FePt-Au,[61] AuNP@CDs,[15] MoS_2 nanosheet[67] and Co_3O_4.[68] This mechanism explains the (i) ping-pong kinetic behavior of the Fe_3O_4@SiO_2-NH_2-Au@$Pd_{0.30}$NPs peroxidase-like activity, (ii) strong affinity for both H_2O_2 and TMB, thus low K_m values, and (iii) the fast colorimetric response was due to the electron transfer mechanism and lack of intermediate radical generation.

An experiment was conducted to confirm oxygen generation as a product of decomposition of H_2O_2 by Fe_3O_4@SiO_2-NH_2-Au@$Pd_{0.30}$NPs. Different concentrations of Fe_3O_4@SiO_2-NH_2-Au@$Pd_{0.30}$NPs were added to a degassed (Ar saturated) solution of 10.0 mM H_2O_2 in acetate buffer. Air bubbles were observed upon addition of Fe_3O_4@SiO_2-NH_2-Au@$Pd_{0.30}$NPs confirming gas evolution. The evolved gas was monitored using dissolved oxygen (DO) meter and an increase in O_2 signal was observed. Figure S7 shows the effect of Fe_3O_4@SiO_2-NH_2-Au@$Pd_{0.30}$NPs concentrations on the generation of dissolved oxygen. The dissolved oxygen concentrations increased with increasing concentration of the Fe_3O_4@SiO_2-NH_2-Au@$Pd_{0.30}$NPs up to about 134.0 μg mL^{-1}. The concentrations of DO remained constant at the addition of higher concentrations (>134.0 μg mL^{-1} of Fe_3O_4@SiO_2-NH_2-Au@$Pd_{0.30}$NPs). The observed increase in O_2 generated suggests that Fe_3O_4@SiO_2-NH_2-Au@$Pd_{0.30}$NPs decomposes H_2O_2 into oxygen and water. The O_2 gas evolution provides evidence that Fe_3O_4@SiO_2-NH_2-Au@$Pd_{0.30}$NPs reduces H_2O_2 following the mechanism as proposed in Scheme 2, that is via an electron transfer process.

Robustness of Peroxidase-Like Activity of Fe_3O_4@SiO_2-NH_2-Au@$Pd_{0.30}$NPs Nanozymes. Figure S8 shows the effect of storage conditions (a) pH (3.0−12.0), (b) temper-

DOI: 10.1021/acsami.9b15123
ACS Appl. Mater. Interfaces 2020, 12, 1973−1987

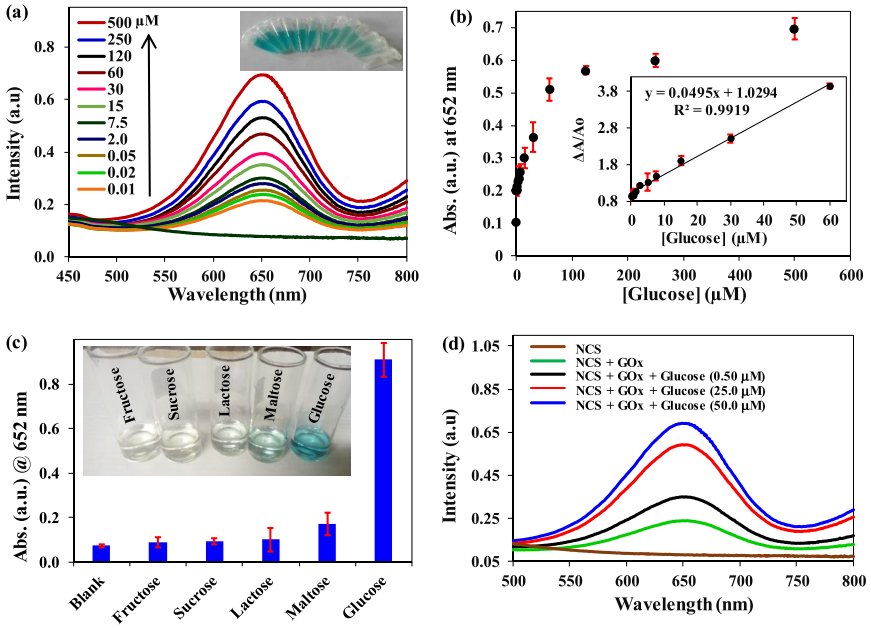

Figure 10. (a) UV−vis absorption spectra (inset images of Eppendorf tubes), (b) the glucose concentration dependence response of Fe_3O_4@SiO_2-NH_2-Au@$Pd_{0.30}$NPs nanozyme glucose sensors, (c) selectivity of glucose amongst other sugars (inset images of vials showing blue color development), and (d) detection of in the absence and presence of glucose (0.50, 25.0, and 50.0 μM) and GOx + newborn calf serum (NCS).

ature and thermal stability (−20−100 °C), (c) NaCl ionic strength (0−100 mM), and (d) long-term storage (weeks) on the peroxidase-like activity of Fe_3O_4@SiO_2-NH_2-Au@$Pd_{0.30}$NPs. Figure S8 shows that there was no significant change in the peroxidase-like activity of the Fe_3O_4@SiO_2-NH_2-Au@$Pd_{0.30}$NPs after storing at different temperatures from −20 to 100 °C. The same was observed for varied pH conditions during storage from pH 3.0 to pH 12.0 in Figure S8b. In comparison, HRP loses its activity at temperatures above 40 °C. The Fe_3O_4@SiO_2-NH_2-Au@$Pd_{0.30}$NPs retained about 95% of its activity, even when subjected to 100 °C storage conditions. The effect of ionic strength of the storage solution was evaluated and showed that the activity was retained from 0 to 100 mM of NaCl in pH 7.0, in Figure S8c. The stability of the Fe_3O_4@SiO_2-NH_2-Au@$Pd_{0.30}$NPs under prolonged storage conditions was also studied. Figure S8d shows that 98% of the peroxidase-like activity was retained after storing at room temperature on a laboratory bench for 3 months. The long-term storage was analyzed every week. The result demonstrated that the Fe_3O_4@SiO_2-NH_2-Au@$Pd_{0.30}$NPs peroxidase-like activity was stable under very harsh environmental conditions not possible with HRP.

Colorimetric Detection of Glucose Using Fe_3O_4@SiO_2-NH_2-Au@$Pd_{0.30}$NPs. The Fe_3O_4@SiO_2-NH_2-Au@$Pd_{0.30}$NPs were evaluated for their potential application as mimics of HRP in glucose detection. The level of glucose in body fluids is of significance in diabetes patients. Therefore, the development of a simple, low-cost, and sensitive sensor for the detection of glucose is of great importance. The Fe_3O_4@SiO_2-NH_2-Au@$Pd_{0.30}$NPs were evaluated for a simple colorimetric glucose sensor when used with glucose oxidase (GOx). Glucose oxidase (GOx) selectively catalyzes the oxidation of glucose to gluconic acid and H_2O_2 in pH 7.0 buffer solution. In the presence of Fe_3O_4@SiO_2-NH_2-Au@$Pd_{0.30}$NPs, the enzymatic generated H_2O_2 facilitated the oxidation of the TMB to its blue TMBDI products, as illustrated in eqs 5 and 6

$$\text{D} - \text{glucose} + \text{O}_2 \xrightarrow{\text{glucose oxidase}} \text{gluconic acid} + \text{H}_2\text{O}_2 \quad (5)$$

$$2\text{H}_2\text{O}_2 + \text{TMB} \xrightarrow{\text{Fe}_3\text{O}_4\ @\text{SiO}_2\ -\text{NH}_2\ -\text{Au@Pd}_{0.30}\ \text{NPs}} \text{TMBDI} + 2\text{H}_2\text{O} + \text{O}_2 \quad (6)$$

The absorbance of the TMBDI at 652 nm was proportional to the concentration of glucose and was used to quantify glucose. Figure 10 shows (a) the UV−vis absorption spectra, (b) the glucose concentration dependence response of Fe_3O_4@SiO_2-NH_2-Au@$Pd_{0.30}$NPs nanozyme glucose sensors, (c) selectivity of glucose amongst other sugars, and (d) detection of glucose in newborn calf serum (NCS). In Figure 10a, an increase in absorption as the concentration of glucose increases was observed at 652 nm. The color dependence of the absorption was also observed in the inset in Figure 10a. Figure 10b shows that the plot of relative change in absorption intensity $\left(\frac{\Delta A_{652}}{A_0} = \frac{A_{glu} - A_o}{A_0}\right)$ increased and reached a plateau at 300 μM showing the Michaelis−Menten relationship. A_{glu} and A_0 represent the absorbance for glucose and blank samples, respectively. The inset in Figure 10b shows that the glucose concentration was linear from 0.010 to 60 μM. The linear regression equation was $\frac{\Delta A_{652}}{A_0} = 0.0495$ [glucose] + 1.03 with R^2 of 0.99. The limit of detection (LoD) and quantification (LoQ) was estimated from the slope (m) of the linear regression and the standard deviation (σ) of the blank samples (1.0 nM, n = 9) as 3 and 10 σ m^{-1}, respectively. The LoD and LoQ were estimated to be 60 and 200 nM, respectively. The LoD was lower than the concentration of glucose in the serum sample of a healthy individual (3.0−8.0 mM) and diabetes patients (9.0−40.0 mM). The Fe_3O_4@SiO_2-NH_2-Au@$Pd_{0.30}$NPs nanozyme glucose sensor showed better or comparable detection limit and linear range when compared with other nanozyme-glucose sensors summarized in Table 1. The high sensitivity of the glucose sensor was ascribed to the

DOI: 10.1021/acsami.9b15123
ACS Appl. Mater. Interfaces 2020, 12, 1973−1987

Table 1. Comparison of Performance of Fe_3O_4@SiO_2-NH_2-Au@$Pd_{0.30}$NPs for Glucose Detection with Other Nanozyme-Based Glucose Biosensors

nanozymes	linear range (μM)	limit of detection (μM)
Fe_3O_4@SiO_2-NH_2-Au@$Pd_{0.30}$NPs	0.010−60	0.060
Fe_3O_4 NPs[17]	50−1000	30.0
CuO−Au alloy[19]	0−30	6.80
Pd−Cu/rGO nanohybrids[34]	0.5−50	0.30
CeO_2/nanotube TiO_2[35]	1−50	6.10
FeSe-Pt@SiO_2 nanocomposite[69]	0.11−227	0.13
Ficin/SiO_2@Fe_3O_4 hybrid[70]	2−10	0.50
Fe_3O_4@SiO_2@Au nanocomposite[71]	5−35	3.00
Cu−Ag/rGO[72]	1−30	3.80
Pt/cube-CeO_2 nanohybrids[73]	0−100	4.10

multiple active catalytic sites and the synergistic effect of the Au@PdNPs. Thus, the developed colorimetric Fe_3O_4@SiO_2-NH_2-Au@$Pd_{0.30}$NPs nanozyme glucose sensor exhibited excellent potential for point-of-care glucose monitoring. The selectivity of the Fe_3O_4@SiO_2-NH_2-Au@$Pd_{0.30}$NPs nanozyme glucose sensor was evaluated by detection of glucose analogues, including sucrose, fructose, maltose, and lactose in solution at a concentration of 25.0 μM for each test. Figure 10c shows that the absorbance of the glucose analogue was significantly lower than that of glucose. Also, the mixture of the glucose and the higher concentrations of the glucose analogues were investigated. As shown in Figure S9, the addition of 100.0 μM of sucrose, lactose, maltose, and fructose has no significant effect on the detection of glucose even though the concentrations of the glucose analogues were 4 times higher than glucose. The results showed that the Fe_3O_4@SiO_2-NH_2-Au@$Pd_{0.30}$NPs nanozyme-GOx system exhibited good selectivity for glucose. The high selectivity could be attributed to the specificity of GOx to glucose and Fe_3O_4@SiO_2-NH_2-Au@$Pd_{0.30}$NPs nanozymes towards H_2O_2. The relative standard deviation for the detection of 25.0 μM of glucose was 1.25% (n = 12), implying excellent reproducibility.

Detection of Glucose in Fetal or Newborn Calf Serum Samples. The detection of glucose concentrations in NCS was studied to mimic the real sample and evaluate the practical applicability of our Fe_3O_4@SiO_2-NH_2-Au@$Pd_{0.30}$NPs nanozyme glucose biosensor. The NCS was spiked with three different glucose concentrations (0.50, 25.0, 50.0 μM). Figure 10d shows the UV−vis spectra obtained from the spiked serum samples. The absorption intensity increased with increasing spiked concentration of glucose in the NCS samples. There was no significant absorption in the solution without the addition of GOx, indicating the selectivity of our sensor for glucose in the serum sample. The concentration of the glucose in the unspiked NCS was below the detection limit of our Fe_3O_4@SiO_2-NH_2-Au@$Pd_{0.30}$NPs nanozyme glucose biosensor. Table 2 shows that the recovery of the glucose biosensor between 94.6 and 110%. The percentage relative standard deviation (% RSD) of three measurements were between 0.50 and 1.50%. The results showed excellent precision and reliability of the Fe_3O_4@SiO_2-NH_2-Au@$Pd_{0.30}$NP nanozyme-GOx biosensor for the detection of glucose in the serum sample.

Reusability of Fe_3O_4@SiO_2-NH_2-Au@$Pd_{0.30}$NP Nanozyme-Based Glucose Detection. Fe_3O_4@SiO_2-NH_2-Au@$Pd_{0.30}$NPs offers additional advantages of reusability due to their magnetic properties. The experiments were conducted by repeating the detection of 50.0 μM glucose for 10 successful cycles. After each measurement, the detection solution was placed on a magnetic rack to separate the Fe_3O_4@SiO_2-NH_2-Au@$Pd_{0.30}$NPs and washed several times with Milli-Q water and ethanol. The recovered Fe_3O_4@SiO_2-NH_2-Au@$Pd_{0.30}$NPs were reused in the next cycle for the detection of glucose. Figure S10 shows that there was no significant change in the activity of Fe_3O_4@SiO_2-NH_2-Au@$Pd_{0.30}$NPs after the 10th successive cycle. About 93% of the peroxidase-like activity of Fe_3O_4@SiO_2-NH_2-Au@$Pd_{0.30}$NPs was retained. The results confirmed the excellent reusability of Fe_3O_4@SiO_2-NH_2-Au@$Pd_{0.30}$NPs for glucose detection, thus being beneficial for practical applications.

Table 2. Detection of Glucose in Spiked Serum Samples Using the Recovery Method[a]

sample	glucose concentration added (μM)	glucose concentration detected (μM)	recovery (%)	% RSD (n = 3)
NCS	0.0	ND		
NCS + 7.5 μM glucose	7.5	7.9	106.0	0.50
NCS + 15.0 μM glucose	15.0	14.2	94.6	1.00
NCS + 30.0 μM glucose	30.0	33.1	110.0	0.90
NCS + 50.0 μM glucose	50.0	52.5	105.0	1.50

[a]ND, non-detectable.

CONCLUSIONS

In conclusion, we have demonstrated that the synthesis of nanomagnet-silica as magnetic supports for Au@PdNPs (Fe_3O_4@SiO_2-NH_2-Au@$Pd_{0.30}$NPs) was achieved and their characterization confirmed the successful synthesis. The peroxidase-like activity of Fe_3O_4@SiO_2-NH_2-Au@$Pd_{0.30}$NPs was investigated and compared with horseradish-peroxidase. The peroxidase-like activity of Fe_3O_4@SiO_2-NH_2-Au@$Pd_{0.30}$NPs was higher than that of HRP and also some peroxidase-like mimetic reported in the literature. The 70% enhancement in the peroxidase-like activity signal was observed for Fe_3O_4@SiO_2-NH_2-Au@$Pd_{0.30}$NPs better than Fe_3O_4@SiO_2-NH_2NPs and the monometallic nanoparticles (Fe_3O_4@SiO_2-NH_2-PdNPs and Fe_3O_4@SiO_2-NH_2-AuNPs). The enhanced Fe_3O_4@SiO_2-NH_2-Au@$Pd_{0.30}$NPs peroxidase-like activity was attributed to the synergistic interaction between AuNPs and Pd-shell. The peroxidase-like activity of Fe_3O_4@SiO_2-NH_2-Au@$Pd_{0.30}$NPs was found to be optimal at pH 5.0 and 30 °C. Kinetic analysis of Fe_3O_4@SiO_2-NH_2-Au@$Pd_{0.30}$NPs showed that the peroxidase-like activity followed typical Michaelis−Menten kinetics. The K_m values were obtained to be 3.50 and 0.060 mM for H_2O_2 and TMB, respectively. The V_{max} (10^{-8} M s^{-1}) values were found to be 6.78 and 8.65 for H_2O_2 and TMB, respectively. The kinetic parameters showed that Fe_3O_4@SiO_2-NH_2-Au@$Pd_{0.30}$NPs had a higher affinity for TMB and H_2O_2 in comparison to HRP. The mechanism of the peroxidase-like activity of Fe_3O_4@SiO_2-NH_2-Au@$Pd_{0.30}$NPs was confirmed to be via an electron transfer between H_2O_2, the nanoparticles, and TMB. Finally, combining Fe_3O_4@SiO_2-NH_2-Au@$Pd_{0.30}$NPs with glucose oxidase, a simple colorimetric nanozyme-glucose biosensor was developed. The biosensor showed good sensitivity and

DOI: 10.1021/acsami.9b15123
ACS Appl. Mater. Interfaces 2020, 12, 1973−1987

selectivity with a linear detection range between 0.010 and 60.0 μM with an LoD of 60 nM and LoQ of 200 nM. To investigate the practical applicability of the proposed glucose sensor, glucose was detected in fetal or newborn calf serum samples accurately using the Fe_3O_4@SiO_2-NH_2-Au@$Pd_{0.30}$NPs nanozyme-glucose biosensor. Compared with HRP, the Fe_3O_4@SiO_2-NH_2-Au@$Pd_{0.30}$NPs can be easily prepared with high stability and reusability with 97% signal retention. Therefore, the proposed Fe_3O_4@SiO_2-NH_2-Au@$Pd_{0.30}$NPs nanozyme-glucose biosensor has great potential in achieving simple, low-cost, rapid, and sensitive point-of-care glucose monitoring.

■ ASSOCIATED CONTENT

Supporting Information

The Supporting Information is available free of charge at https://pubs.acs.org/doi/10.1021/acsami.9b15123.

Detailed information about the experimental procedures for the synthesis of Fe_3O_4@SiO_2-NH_2-Au@PdNPs, evaluation of peroxidase-like activity, kinetic parameter, and method for glucose detection; XRD pattern of Fe_3O_4@SiO_2-NH_2-Au@PdNPs synthesized with different H_2PdCl_4 concentrations, EDS spectra of the different stage of materials during the synthesis steps; peroxidase-like activity of different nanoparticles; UV−vis absorption spectra of leaching solution before and after incubation in an acid buffer solution; effect of temperature (−20−100 °C), pH (3.0−12.0), ionic strength NaCl (0.0−100.0 mM), and long term stability of Fe_3O_4@SiO_2-NH_2-Au@$Pd_{0.30}$NPs; selectivity studies of Fe_3O_4@SiO_2-NH_2-Au@$Pd_{0.30}$NP-based glucose detection and other sugars (PDF)

■ AUTHOR INFORMATION

Corresponding Author

*E-mail: p.mashazi@ru.ac.za.

ORCID

Philani Mashazi: 0000-0003-4815-6146

Notes

The authors declare no competing financial interest.

■ ACKNOWLEDGMENTS

The research reported in this publication was supported by the South African Medical Research Council under a Self-Initiated Research Grant (MRC-SIR); National Research Foundation through Thuthuka Post-PhD Programme (NRF-TTK UID—842230), Rated Incentive funding (UID 96001); and Rhodes University Research Council and Researcher Development Grant (RDG P5/17/2015). AO acknowledges TWAS/NRF for the PhD scholarship.

■ REFERENCES

(1) Wu, J.; Wang, X.; Wang, Q.; Lou, Z.; Li, S.; Zhu, Y.; Qin, L.; Wei, H. Nanomaterials with Enzyme-like Characteristics (Nanozymes): Next-Generation Artificial Enzymes (II). *Chem. Soc. Rev.* **2019**, *48*, 1004−1076.

(2) Lin, Y.; Ren, J.; Qu, X. Catalytically Active Nanomaterials: A Promising Candidate for Artificial Enzymes. *Acc. Chem. Res.* **2014**, *47*, 1097−1105.

(3) Dong, W.; Zhuang, Y.; Li, S.; Zhang, X.; Chai, H.; Huang, Y. High Peroxidase-like Activity of Metallic Cobalt Nanoparticles Encapsulated in Metal−Organic Frameworks Derived Carbon for Biosensing. *Sens. Actuators, B* **2018**, *255*, 2050−2057.

(4) Wang, X.; Cao, W.; Qin, L.; Lin, T.; Chen, W.; Lin, S.; Yao, J.; Zhao, X.; Zhou, M.; Hang, C.; Wei, H. Boosting the Peroxidase-like Activity of Nanostructured Nickel by Inducing Its 3+ Oxidation State in $LaNiO_3$ Perovskite and Its Application for Biomedical Assays. *Theranostics* **2017**, *7*, 2277−2286.

(5) Wang, Z.; Yang, X.; Yang, J.; Jiang, Y.; He, N. Peroxidase-like Activity of Mesoporous Silica Encapsulated Pt Nanoparticle and Its Application in Colorimetric Immunoassay. *Anal. Chim. Acta* **2015**, *862*, 53−63.

(6) He, W.; Liu, Y.; Yuan, J.; Yin, J. J.; Wu, X.; Hu, X.; Zhang, K.; Liu, J.; Chen, C.; Ji, Y.; Guo, Y. Au@Pt Nanostructures as Oxidase and Peroxidase Mimetics for Use in Immunoassays. *Biomaterials* **2011**, *32*, 1139−1147.

(7) Li, S.; Wang, L.; Zhang, X.; Chai, H.; Huang, Y. A Co,N Co-Doped Hierarchically Porous Carbon Hybrid as a Highly Efficient Oxidase Mimetic for Glutathione Detection. *Sens. Actuators, B* **2018**, *264*, 312−319.

(8) Mu, J.; Wang, Y.; Zhao, M.; Zhang, L. Intrinsic Peroxidase-like Activity and Catalase-like Activity of Co_3O_4 Nanoparticles. *Chem. Commun.* **2012**, *48*, No. 2540.

(9) Bhagat, S.; Srikanth Vallabani, N. V.; Shutthanandan, V.; Bowden, M.; Karakoti, A. S.; Singh, S. Gold Core/Ceria Shell-Based Redox Active Nanozyme Mimicking the Biological Multienzyme Complex Phenomenon. *J. Colloid Interface Sci.* **2018**, *513*, 831−842.

(10) Cao, J.-C.; Jiang, X.; Zhang, H.; Croley, T. R.; Yin, J. J. Mimicking Horseradish Peroxidase and Oxidase Using Ruthenium Nanomaterials. *RSC Adv.* **2017**, *7*, 52210−52217.

(11) Gao, L.; Zhuang, J.; Nie, L.; Zhang, J.; Zhang, Y.; Gu, N.; Wang, T.; Feng, J.; Yang, D.; Perrett, S.; Yan, X. Intrinsic Peroxidase-like Activity of Ferromagnetic Nanoparticles. *Nat. Nanotechnol.* **2007**, *2*, 577−583.

(12) Zhou, N.; Zou, S.; Zou, L.; Shen, R.; Zhou, Y.; Ling, L. Peroxidase-like Activity of Palladium Nanoparticles on Hydrogen-Bond Supramolecular Structures over a Broader PH Range and Their Application in Glucose Sensing. *Can. J. Chem.* **2019**, *97*, 317−323.

(13) Shi, W.; Fan, H.; Ai, S.; Zhu, L. Honeycomb-like Nitrogen-Doped Porous Carbon Supporting Pt Nanoparticles as Enzyme Mimic for Colorimetric Detection of Cholesterol. *Sens. Actuators, B* **2015**, *221*, 1515−1522.

(14) Jiang, H.; Chen, Z.; Cao, H.; Huang, Y. Peroxidase-like Activity of Chitosan Stabilized Silver Nanoparticles for Visual and Colorimetric Detection of Glucose. *Analyst* **2012**, *137*, 5560−5564.

(15) Zheng, C.; Ke, W.; Yin, T.; An, X. Intrinsic Peroxidase-like Activity and the Catalytic Mechanism of Gold@carbon Dots Nanocomposites. *RSC Adv.* **2016**, *6*, 35280−35286.

(16) Alizadeh, N.; Salimi, A.; Hallaj, R. Mimicking Peroxidase Activity of $Co_2(OH)_2CO_3$-CeO_2 nanocomposite for Smartphone Based Detection of Tumor Marker Using Paper-Based Microfluidic Immunodevice. *Talanta* **2018**, *189*, 100−110.

(17) An, Q.; Sun, C.; Li, D.; Xu, K.; Guo, J.; Wang, C. Peroxidase-like Activity of Fe_3O_4@carbon Nanoparticles Enhances Ascorbic Acid-Induced Oxidative Stress and Selective Damage to PC-3 Prostate Cancer Cells. *ACS Appl. Mater. Interfaces* **2013**, *5*, 13248−13257.

(18) Nagvenkar, A. P.; Gedanken, A. $Cu_{0.89}Zn_{0.11}O$, A New Peroxidase-Mimicking Nanozyme with High Sensitivity for Glucose and Antioxidant Detection. *ACS Appl. Mater. Interfaces* **2016**, *8*, 22301−22308.

(19) Mvango, S.; Mashazi, P. Synthesis, Characterization of Copper Oxide-Gold Nanoalloys and Their Peroxidase-like Activity towards Colorimetric Detection of Hydrogen Peroxide and Glucose. *Mater. Sci. Eng., C* **2019**, *96*, 814−823.

(20) Meilikhov, M.; Yusenko, K.; Esken, D.; Turner, S.; Van Tendeloo, G.; Fischer, R. A. Metals@MOFs - Loading MOFs with Metal Nanoparticles for Hybrid Functions. *Eur. J. Inorg. Chem.* **2010**, 3701−3714.

(21) Zheng, H. Q.; Liu, C. Y.; Zeng, X. Y.; Chen, J.; Lü, J.; Lin, R. G.; Cao, R.; Lin, Z. J.; Su, J. W. MOF-808: A Metal-Organic

DOI: 10.1021/acsami.9b15123
ACS Appl. Mater. Interfaces 2020, 12, 1973−1987

Framework with Intrinsic Peroxidase-Like Catalytic Activity at Neutral pH for Colorimetric Biosensing. *Inorg. Chem.* **2018**, *57*, 9096−9104.
(22) Li, H.; Xu, Q.; Shu, Y.; Hu, X.; Chen, J. Nickel Metal-Organic Framework 2D Nanosheets with Enhanced Peroxidase Nanozyme Activity for Colorimetric Detection of H_2O_2. *Talanta* **2018**, *189*, 254−261.
(23) Li, S.; Liu, X.; Chai, H.; Huang, Y. Recent Advances in the Construction and Analytical Applications of Metal-Organic Frameworks-Based Nanozymes. *TrAC - Trends Anal. Chem.* **2018**, *105*, 391−403.
(24) Lin, L.; Song, X.; Chen, Y.; Rong, M.; Zhao, T.; Wang, Y.; Jiang, Y.; Chen, X. Intrinsic Peroxidase-like Catalytic Activity of Nitrogen-Doped Graphene Quantum Dots and Their Application in the Colorimetric Detection of H_2O_2 and Glucose. *Anal. Chim. Acta* **2015**, *869*, 89−95.
(25) Garg, B.; Bisht, T.; Ling, Y. C. Graphene-Based Nanomaterials as Efficient Peroxidase Mimetic Catalysts for Biosensing Applications: An Overview. *Molecules* **2015**, *20*, 14155−14190.
(26) Zheng, A. X.; Cong, Z. X.; Wang, J. R.; Li, J.; Yang, H. H.; Chen, G. N. Highly-Efficient Peroxidase-like Catalytic Activity of Graphene Dots for Biosensing. *Biosens. Bioelectron.* **2013**, *49*, 519−524.
(27) Shin, H. Y.; Park, T. J.; Kim, M. Il. Recent Research Trends and Future Prospects in Nanozymes. *J. Nanomater.* **2015**, *2015*, 1−11.
(28) Kim, M. S.; Cho, S.; Joo, S. H.; Lee, J.; Kwak, S. K.; Kim, M. Il.; Lee, J. N- and B-Codoped Graphene: A Strong Candidate to Replace Natural Peroxidase in Sensitive and Selective Bioassays. *ACS Nano* **2019**, *13*, 4312−4321.
(29) Singh, S. Catalytically Active Nanomaterials: Artificial Enzymes of Next Generation. *Nanosci. Technol. Open Access* **2017**, *5*, 1−6.
(30) He, W.; Han, X.; Jia, H.; Cai, J.; Zhou, Y.; Zheng, Z. AuPt Alloy Nanostructures with Tunable Composition and Enzyme-like Activities for Colorimetric Detection of Bisulfide. *Sci. Rep.* **2017**, *7*, No. 40103.
(31) Su, L.; Dong, W.; Wu, C.; Gong, Y.; Zhang, Y.; Li, L.; Mao, G.; Feng, S. The Peroxidase and Oxidase-like Activity of $NiCo_2O_4$ Mesoporous Spheres: Mechanistic Understanding and Colorimetric Biosensing. *Anal. Chim. Acta* **2017**, *951*, 124−132.
(32) Qi, C.; Cai, S.; Wang, X.; Li, J.; Lian, Z.; Sun, S.; Yang, R.; Wang, C. Enhanced Oxidase/Peroxidase-like Activities of Aptamer Conjugated MoS_2/PtCu Nanocomposites and Their Biosensing Application. *RSC Adv.* **2016**, *6*, 54949−54955.
(33) Hu, Z.; Dai, Z.; Hu, X.; Chen, K.; Gao, C.; Zheng, X.; Yu, Y. Synthesis of PB@FePt Hybrid Nanoparticles with Peroxidase-Mimicking Activity for Colorimetric Determination of Hydrogen Peroxide in Living Cells. *Anal. Methods* **2019**, *11*, 677−683.
(34) Darabdhara, G.; Boruah, P. K.; Das, M. R. Colorimetric Determination of Glucose in Solution and via the Use of a Paper Strip by Exploiting the Peroxidase and Oxidase Mimicking Activity of Bimetallic Cu-Pd Nanoparticles Deposited on Reduced Graphene Oxide, Graphitic Carbon Nitride, or MoS_2 Nanosh. *Microchim. Acta* **2019**, *186*, No. 11939.
(35) Zhao, H.; Dong, Y.; Jiang, P.; Wang, G.; Zhang, J. Highly Dispersed CeO_2 on TiO_2 Nanotube: A Synergistic Nanocomposite with Superior Peroxidase-like Activity. *ACS Appl. Mater. Interfaces* **2015**, *7*, 6451−6461.
(36) Vogt, C.; Toprak, M. S.; Muhammed, M.; Laurent, S.; Bridot, J. L.; Müller, R. N. High Quality and Tuneable Silica Shell-Magnetic Core Nanoparticles. *J. Nanopart. Res.* **2010**, *12*, 1137−1147.
(37) Ding, H. L.; Zhang, Y. X.; Wang, S.; Xu, J. M.; Xu, S. C.; Li, G. H. Fe_3O_4@SiO_2 Core/Shell Nanoparticles: The Silica Coating Regulations with a Single Core for Different Core Sizes and Shell Thicknesses. *Chem. Mater.* **2012**, *24*, 4572−4580.
(38) Chen, D.; Li, J.; Cui, P.; Liu, H.; Yang, J. Gold-Catalyzed Formation of Core−Shell Gold−Palladium Nanoparticles with Palladium Shells up to Three Atomic Layers. *J. Mater. Chem. A* **2016**, *4*, 3813−3821.
(39) Liu, J.; He, F.; Gunn, T. M.; Zhao, D.; Roberts, C. B. Precise Seed-Mediated Growth and Size-Controlled Synthesis of Palladium Nanoparticles Using a Green Chemistry Approach. *Langmuir* **2009**, *25*, 7116−7128.
(40) Leng, W.; Pati, P.; Vikesland, P. J. Room Temperature Seed Mediated Growth of Gold Nanoparticles: Mechanistic Investigations and Life Cycle Assesment. *Environ. Sci. Nano* **2015**, *2*, 440−453.
(41) Lopez-Sanchez, J. A.; Dimitratos, N.; Miedziak, P.; Ntainjua, E.; Edwards, J. K.; Morgan, D.; Carley, A. F.; Tiruvalam, R.; Kiely, C. J.; Hutchings, G. J. Au−Pd Supported Nanocrystals Prepared by a Sol Immobilisation Technique as Catalysts for Selective Chemical Synthesis. *Phys. Chem. Chem. Phys.* **2008**, *10*, 1921−1930.
(42) Song, H.; Luo, Z.; Liu, M.; Zhang, G.; Peng, W.; Wang, B.; Zhu, Y. Centrifugal Deposited Au−Pd Core-Shell Nanoparticle Film for Room-Temperature Optical Detection of Hydrogen Gas. *Sensors* **2018**, *18*, No. 1448.
(43) Yenagi, J.; Nandurkar, A. R.; Tonannavar, J. 2-Methoxyphenyl Isocyanate and 2-Methoxyphenyl Isothiocyanate: Conformers, Vibration Structure and Multiplet Fermi Resonance. *Spectrochim. Acta, Part A* **2012**, *91*, 261−268.
(44) Yu, J.; Wang, B. Effect of Calcination Temperature on Morphology and Photoelectrochemical Properties of Anodized Titanium Dioxide Nanotube Arrays. *Appl. Catal., B* **2010**, *94*, 295−302.
(45) Radnik, J.; Mohr, C.; Claus, P. On the Origin of Binding Energy Shifts of Core Levels of Supported Gold Nanoparticles and Dependence of Pretreatment and Material Synthesis. *Phys. Chem. Chem. Phys.* **2003**, *5*, 172−177.
(46) Hardiansyah, A.; Chen, A. Y.; Liao, H. L.; Yang, M. C.; Liu, T. Y.; Chan, T. Y.; Tsou, H. M.; Kuo, C. Y.; Wang, J. K.; Wang, Y. L. Core-Shell of FePt@SiO_2-Au Magnetic Nanoparticles for Rapid SERS Detection. *Nanoscale Res. Lett.* **2015**, *10*, 2−10.
(47) Castillo, C.; Buono-Core, G.; Manzur, C.; Yutronic, N.; Sierpe, R.; Cabello, G.; Chornik, B. Molybdenum Trioxide Thin Films Doped With Gold Nanoparticles Grown By a Sequential Methodology: Photochemical Metal-Organic Deposition (PMOD) and Dc-Magnetron Sputtering. *J. Chil. Chem. Soc.* **2016**, *61*, 2816−2820.
(48) Ryabenkova, Y.; He, Q.; Miedziak, P. J.; Dummer, N. F.; Taylor, S. H.; Carley, A. F.; Morgan, D. J.; Dimitratos, N.; Willock, D. J.; Bethell, D.; Knight, D. W.; Chadwick, D.; Kiely, C. J.; Hutchings, G. J. The Selective Oxidation of 1,2-Propanediol to Lactic Acid Using Mild Conditions and Gold-Based Nanoparticulate Catalysts. *Catal. Today* **2013**, *203*, 139−145.
(49) Nemšák, S.; Skála, T.; Libra, J.; Mašek, K.; Cabala, M.; Matolín, V. The Growth of Au/Pd on Alumina/Cu-Al System. *J. Phys. Conf. Ser.* **2008**, *100*, 8−12.
(50) Wang, D.; Cui, X.; Xiao, Q.; Hu, Y.; Wang, Z.; Yiu, Y. M.; Sham, T. K. Electronic Behaviour of Au-Pt Alloys and the 4f Binding Energy Shift Anomaly in Au Bimetallics- X-Ray Spectroscopy Studies. *AIP Adv.* **2018**, *8*, No. 065210.
(51) Lee, Y. S.; Jeon, Y.; Chung, Y. D.; Lim, K. Y.; Whang, C. N.; Oh, S. J. Charge Redistribution and Electronic Behavior in Pd-Au Alloys. *J. Korean Phys. Soc.* **2000**, *37*, 451−455.
(52) Bhardwaj, M.; Sharma, H.; Paul, S.; Clark, J. H. Fe_3O_4@SiO_2/EDAC-Pd(0) as a Novel and Efficient Inorganic/Organic Magnetic Composite: Sustainable Catalyst for the Benzylic C-H Bond Oxidation and Reductive Amination under Mild Conditions. *New J. Chem.* **2016**, *40*, 4952−4961.
(53) Zhang, S.; Wang, H.; Tang, L.; Li, M.; Y; Tian, J.; Cui, Y.; Han, J.; Zhu, X.; Liu, X. Sub 1 nm Aggregation-Free AuPd Nanocatalysts Confined inside Amino-Functionalized Organosilica Nanotubes for Visible-Light-Driven Hydrogen Evolution from Formaldehyde. *Appl. Catal., B* **2018**, *220*, 303−313.
(54) Chen, D.; Li, C.; Liu, H.; Ye, F.; Yang, J. Core-Shell Au@Pd Nanoparticles with Enhanced Catalytic Activity for Oxygen Reduction Reaction via Core-Shell Au@Ag/Pd Constructions. *Sci. Rep.* **2015**, *5*, No. 11949.
(55) Miller, H. A.; Bellini, M.; Vizza, F.; Hasenöhrl, C.; Tilley, R. D. Carbon Supported Au−Pd Core-Shell Nanoparticles for Hydrogen

DOI: 10.1021/acsami.9b15123
ACS Appl. Mater. Interfaces 2020, 12, 1973−1987

Production by Alcohol Electroreforming. *Catal. Sci. Technol.* **2016**, *6*, 6870−6878.
(56) Bi, C.; Feng, C.; Miao, T.; Song, Y.; Wang, D.; Xia, H. Understanding the Effect of Ultrathin AuPd Alloy Shells of Irregularly Shaped Au@AuPd Nanoparticles with High-Index Facets on Enhanced Performance of Ethanol Oxidation. *Nanoscale* **2015**, *7*, 20105−20116.
(57) Karaseva, E. I.; Losev, Y. P.; Metelitsa, D. I. Peroxidase-Catalyzed Oxidation of 3,3′,5,5′ -Tetramethylbenzidine in the Presence of 2,4-Dinitrosoresorcinol and Polydisulfide Derivatives of Resorcinol and 2,4-Dinitrosoresorcinol. *Russ. J. Bioorg. Chem.* **2002**, *28*, 128−135.
(58) Yang, Y.; Shen, D.; Long, Y.; Xie, Z.; Zheng, H. Intrinsic Peroxidase-like Activity of Ficin. *Sci. Rep.* **2017**, *7*, No. 43141.
(59) Nicell, J. A.; Wright, H. A Model of Peroxidase Activity with Inhibition by Hydrogen Peroxide. *Enzyme Microb. Technol.* **1997**, *21*, 302−310.
(60) Song, Y.; Qu, K.; Zhao, C.; Ren, J.; Qu, X. Graphene Oxide: Intrinsic Peroxidase Catalytic Activity and Its Application to Glucose Detection. *Adv. Mater.* **2010**, *22*, 2206−2210.
(61) Ding, Y.; Yang, B.; Liu, H.; Liu, Z.; Zhang, X.; Zheng, X.; Liu, Q. FePt-Au Ternary Metallic Nanoparticles with the Enhanced Peroxidase-like Activity for Ultrafast Colorimetric Detection of H_2O_2. *Sens. Actuators, B* **2018**, *259*, 775−783.
(62) Tan, H.; Li, Q.; Zhou, Z.; Ma, C.; Song, Y.; Xu, F.; Wang, L. A Sensitive Fluorescent Assay for Thiamine Based on Metal-Organic Frameworks with Intrinsic Peroxidase-like Activity. *Anal. Chim. Acta* **2015**, *856*, 90−95.
(63) Su, L.; Feng, J.; Zhou, X.; Ren, C.; Li, H.; Chen, X. Colorimetric Detection of Urine Glucose Based $ZnFe_2O_4$ Magnetic Nanoparticles. *Anal. Chem.* **2012**, *84*, 5753−5758.
(64) Chen, W.; Chen, J.; Liu, A. L.; Wang, L. M.; Li, G. W.; Lin, X. H. Peroxidase-Like Activity of Cupric Oxide Nanoparticle. *ChemCatChem* **2011**, *3*, 1151−1154.
(65) Fakhri, N.; Salehnia, F.; Beigi, S. M.; Aghabalazadeh, S.; Hosseini, M.; Ganjali, M. R. Enhanced Peroxidase-like Activity of Platinum Nanoparticles Decorated on Nickel- and Nitrogen-Doped Graphene Nanotubes : Colorimetric Detection of Glucose. *Michrochim. Acta* **2019**, *186*, 1−9.
(66) Gao, Z.; Xu, M.; Lu, M.; Chen, G.; Tang, D. Urchin-like (Gold Core)@(Platinum Shell) Nanohybrids: A Highly Efficient Peroxidase-Mimetic System for in Situ Amplified Colorimetric Immunoassay. *Biosens. Bioelectron.* **2015**, *70*, 194−201.
(67) Han, L.; Shi, J.; Liu, A.; Liu, A. Novel Biotemplated MnO_2 1D Nanozyme with Controllable Peroxidase-like Activity and Unique Catalytic Mechanism and Its Application for Glucose Sensing. *Sens. Actuators, B* **2017**, *252*, 919−926.
(68) Mu, J.; Wang, Y.; Zhao, M.; Zhang, L. Intrinsic Peroxidase-like Activity and Catalase-like Activity of Co_3O_4 Nanoparticles. *Chem. Commun.* **2012**, *48*, 2540−2542.
(69) Qiao, F.; Wang, Z.; Xu, K.; Ai, S. Double Enzymatic Cascade Reactions within FeSe-Pt@SiO_2 Nanospheres: Synthesis and Application toward Colorimetric Biosensing of H_2O_2 and Glucose. *Analyst* **2015**, *140*, 6684−6691.
(70) Pang, Y.; Huang, Z.; Yang, Y.; Long, Y.; Zheng, H. Colorimetric Detection of Glucose Based on Ficin with Peroxidase-like Activity. *Spectrochim. Acta, Part A* **2018**, *189*, 510−515.
(71) Luo, S.; Liu, Y.; Rao, H.; Wang, Y.; Wang, X. Fluorescence and Magnetic Nanocomposite Fe_3O_4@SiO_2@Au MNPs as Peroxidase Mimetics for Glucose Detection. *Anal. Biochem.* **2017**, *538*, 26−33.
(72) Darabdhara, G.; Sharma, B.; Das, M. R.; Boukherroub, R.; Szunerits, S. Cu-Ag Bimetallic Nanoparticles on Reduced Graphene Oxide Nanosheets as Peroxidase Mimic for Glucose and Ascorbic Acid Detection. *Sens. Actuators, B* **2017**, *238*, 842−851.
(73) Li, Z.; Yang, X.; Yang, Y.; Tan, Y.; He, Y.; Liu, M.; Liu, X.; Yuan, Q. Peroxidase-Mimicking Nanozyme with Enhanced Activity and High Stability Based on Metal−Support Interactions. *Chem. - Eur. J.* **2018**, *24*, 409−415.

DOI: 10.1021/acsami.9b15123
ACS Appl. Mater. Interfaces 2020, 12, 1973−1987